Measuring and Observing the Ocean Renewable Energy Resource

David Christie, Simon Neill

July 6, 2021

Contents

11.1 Introduction 3
11.2 Introduction to Modelling 4
11.2.1 Discretization in Space and Time 6
11.2.2 Numerical Methods 10
11.2.3 Calibration and Validation 13
11.3 Tidal Energy Resource Characterization 14
11.3.1 Measuring the Tidal Resource 15
11.3.2 Modelling the Tidal Resource 20
11.4 Wave Energy Resource Characterisation 29
11.4.1 Measuring the Wave Resource 29
11.4.2 Modelling the Wave Resource 38

11.1 Introduction

Throughout a renewable energy project, a developer must be confident in their understanding of the available resource. They will need information about the power yield, directionality, spatial and temporal variability and extreme values, to an appropriate level of fidelity for each stage of the development process. A robust prediction of yield over decadal scales with quantified uncertainty is essential for technical and financial decision making. Spatial variability must be properly captured for optimal location of devices, from initial site selection to detailed "micro-siting" of individual devices within an array, and for determining environmental impacts. Wave spectral information – either through parameters such as energy period and significant waveheight, or more detailed directional spectra – are required for tuning and optimisation of wave energy converters, with seastate statistics to be used in conjunction with the device power matrix to predict in situ performance. Tidal stream devices require accurate statistical characterisation of current flow speed, direction and vertical profile.

Informed deployment decisions require sensor deployment for a detailed characterisation of the resource at fine temporal scales, plus numerical modelling to extend the picture in space and time. However, in situ measurement campaigns are costly, particularly in the environments which, by their very nature, are characterised by the strong tidal currents or energetic waves that are suitable

for generating electricity, and may require a lengthy deployment to capture variability. Similarly, setting up a bespoke numerical model with all the required input data can be a challenging exercise. Therefore, prior to devoting time and resources to detailed local characterisation, the initial site selection stage can begin with a desk-based survey of existing datasets. Global wave or current models such as WAVEWATCH III hindcast reanalysis [30] and the ECMWF ERA-5 Global Reanalysis [17] (for waves) or TPXO9 [13] (for tides) will give a useful overview, albeit at coarse spatial resolution. Regional datasets can offer additional resource information for renewable developers. For example, in the UK, the ABPmer Atlas of UK Marine Renewable Energy Resources [1] provides information on the spatial distribution of wave power and depth-averaged spring tidal currents, while Admiralty Charts provide information such as the distribution of bathymetric contours, tidal range, and spring and neap current speeds (and directions) at specific points known as *tidal diamonds*. Datasets from existing nearby sensors may also offer a flavour of the available resource, though their locations are unlikely to be optimally selected for renewable energy applications. In the United Kingdom, WaveNet (Fig. 11.1) publish data from their collection of 99 wave buoys although, since the infrastructure was primarily intended to monitor flood risk to coastal communities and infrastructure, there are few buoys deployed in the west coast of Scotland where the UK's most energetic wave conditions can be found.

Beyond initial scoping exercises, a suitably detailed understanding of resource, variability, uncertainty and site conditions for device deployment requires a combination of modelling and in situ measurement for the location in question. Direct measurement is essential to quantify the resource at high temporal resolution, without the assumptions that are necessary when parametrising numerical simulations, and allows detailed exploration of site-specific hydrodynamic conditions and extrema. Modelling is vital to develop a long-term characterisation of the resource, including spatial and temporal variation. Although wave and tidal studies will differ in terms of physics, they share a common underlying methodology, which will be described in Section 11.2. A robust model, optimally configured to local conditions with properly quantified error estimations, requires strategically placed sensors for validation (and calibration if required) with measured field data. Although they differ in terms of resolution and fidelity, both (pre-)feasibility and design level resource quantification require such an integrated approach, combining modelling and field measurement. The tidal resource assessment procedure will be described in more detail in Section 11.3. A corresponding treatment of wave resource characterization will follow in Section 11.4.

11.2 Introduction to Modelling

Ocean modelling is a commonly used and economical tool in resource characterisation, which can be used to generate long time series or understand how the resource varies under hypothetical scenarios such as climate change, extreme

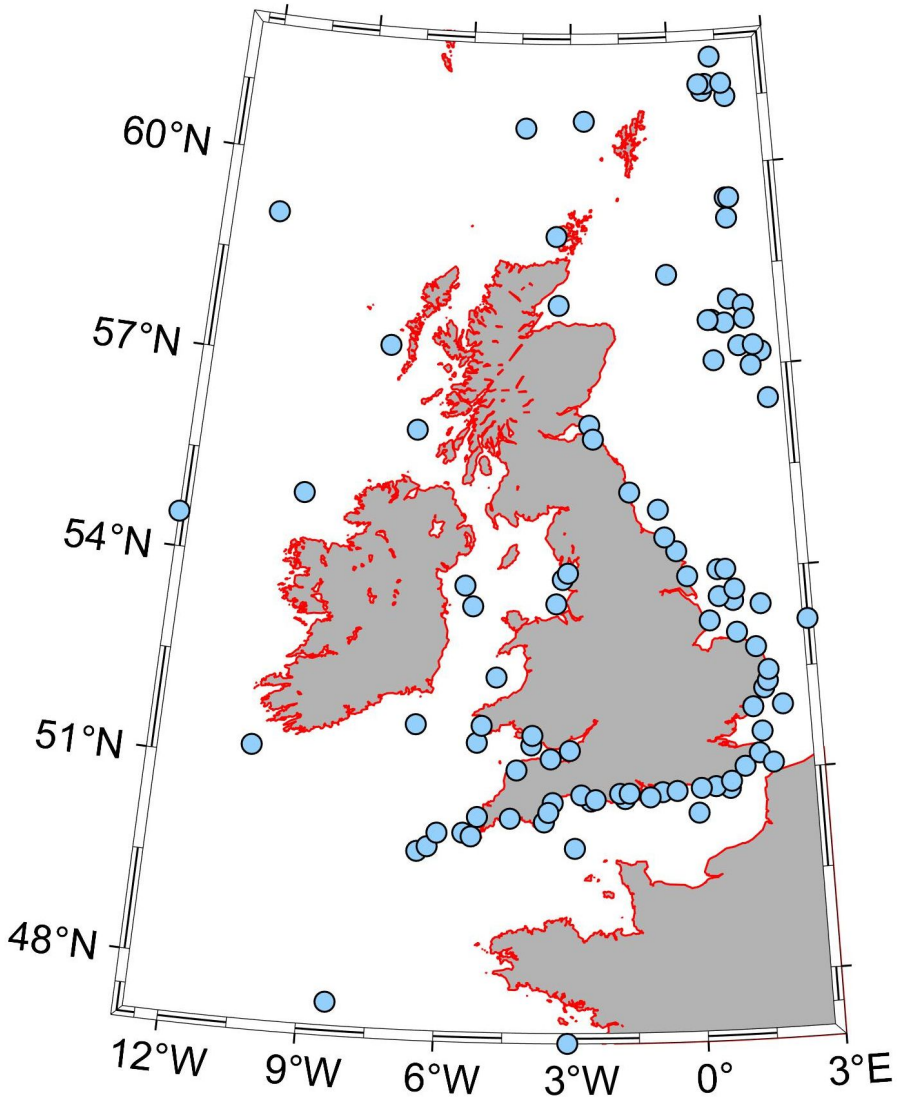

Figure 11.1: The 99 stations that comprise the UK wave network 'WaveNet'. Note the paucity of wave buoys in the energetic waters to the west of Scotland.

events, or how the resource will be influenced by energy extraction. Ocean models can be used at all stages of project development, with early scoping stages laying the groundwork for detailed site selection and investment in field campaigns and later stages ensuring that the resource is accurately understood and optimally harnessed. However, it should be stressed that models are only as good as their input data[1], and that it is always important to parameterise and validate such models with in situ measurements.

A wave or tidal model is a representation of the behaviour of waves or currents in terms of a set of governing equations, with appropriate initial or boundary conditions, and reasonable parametrisations of the physical processes involved therein. This model is then implemented in a simulation, where a numerical differential equation solver will track the evolution of the system. This involves suitable discretisation so that the underlying continuum equations can be transformed to a suitable computational grid.

There is a vast array of ocean models, and a wide range of ways in which they can be categorised. There are many places we could begin this classification but, since it is of much interest to wave and tidal resource characterisation, we begin by considering how the model domain is discretized, differentiating between structured and unstructured meshes.

11.2.1 Discretization in Space and Time

Horizontal Grid Types

In a *structured grid*, all grid lines are orientated regularly so that, in a two-dimensional case, the coordinate transformations of curvilinear lines results in a square (Fig. 11.2a). In contrast, *unstructured grids* are not restricted to a particular orientation (Fig. 11.2b); however, this more flexible grid can be more complex to deal with, and a poorly configured mesh can introduce computational bottlenecks or instabilities. The advantage of a structured grid is its simplicity and ease of pre- and post-processing; however, to achieve a desired resolution (for example, to resolve the curved geometry shown in Fig. 11.2a), it is necessary to use a constant and high resolution grid throughout the computational domain. With an unstructured grid, the high resolution coverage can be restricted to areas where it is required while excluding areas of land may reduce storage (Fig. 11.2b).

Within the context of ocean energy, due to its ability to accommodate a wide range of scales within a single model domain, for example a regional model which incorporates a tidal energy array within a narrow strait, unstructured meshes tend to be favoured for resource assessment. However, many ocean models, particularly 3D models, which simulate a wide range of physical processes, are based on a structured mesh. Under such circumstances, a sequence of nested models, with increasing grid resolution from outer to inner nests, will be required. In general, structured meshes tend to be favoured for larger scale ocean modelling applications.

[1] GIGO – Garbage In, Garbage Out

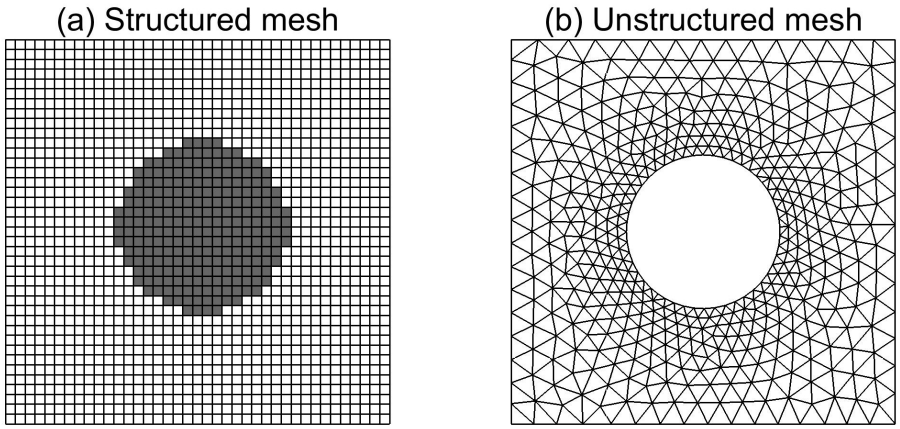

Figure 11.2: (a) Structured and (b) unstructured horizontal mesh.

Vertical Grid Types

In addition to horizontal resolution, three-dimensional (3D) models must also consider how to discretise the space in the vertical direction. The simplest vertical coordinate system, known as *z-coordinates*, has been used by the ocean modelling community for many decades. The z-coordinate scheme divides the entire water column into a fixed number of depth levels, and these can be distributed to provide higher resolution in any particular region, such as the surface layer (Fig. 11.3a). The disadvantage of the z-coordinate system, as demonstrated in Fig. 11.3a, is that it has problems dealing with large changes in bathymetry, which can lead to unrealistic vertical velocities near the bed. Increasing the number of vertical levels will improve the representation of near-bottom flow, but at increased computational cost. This problem is overcome by the sigma coordinate scheme (also known as terrain following coordinate system), where the vertical coordinate follows the bathymetry (Fig. 11.3b). The *sigma coordinate* system results in the same number of vertical grid points throughout the computational domain, regardless of large changes in bathymetry. The sigma levels do not have to be evenly distributed throughout the water column and could, for example, be more closely spaced near the surface and bed, allowing boundary layers to be better resolved throughout the domain. However, one disadvantage of sigma coordinates is that they can lead to difficulties when dealing with sharp changes in bathymetry from one grid point to another. This can lead to pressure gradient errors, resulting in unrealistic flows [24]. Increased horizontal resolution, or bathymetric smoothing, alleviates the problem.

Time step

One of the most important considerations in model setup is the time step of the simulation. When selecting a model time step, it is important to consider both

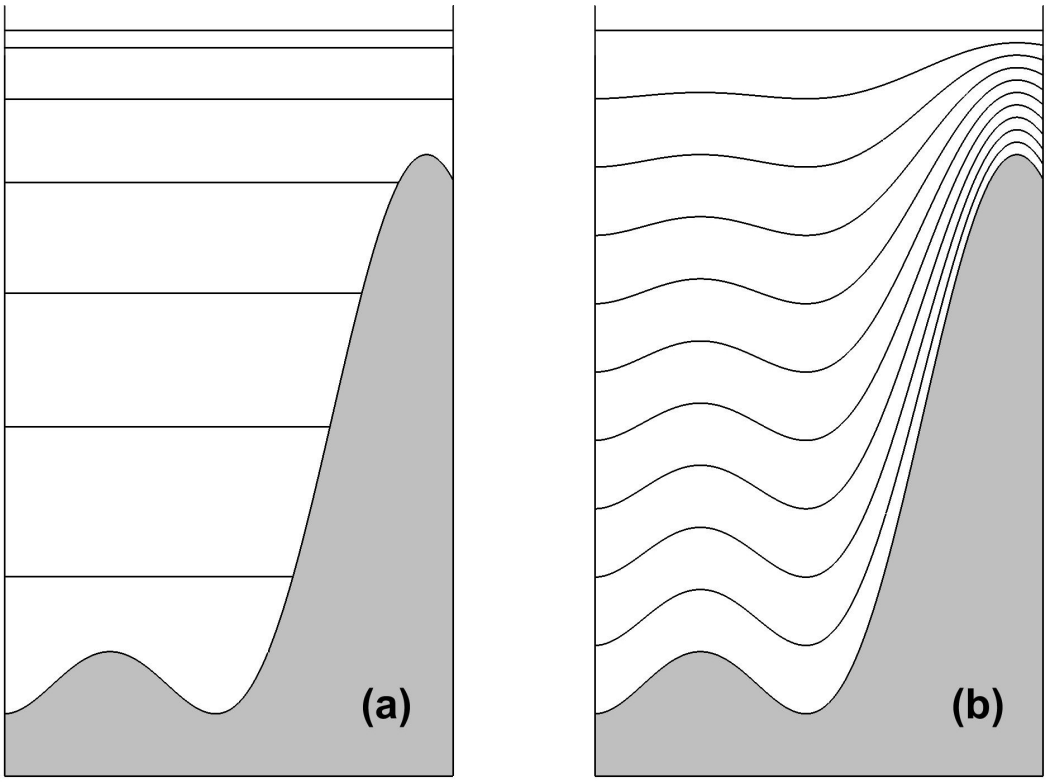

Figure 11.3: Vertical mesh for (a) z-coordinate, and (b) sigma coordinate systems

accuracy and *stability*. For example, the model time step must be sufficiently small to capture temporal variability in the physical process. An example of this is shown in Fig. 11.4 where, graphically, a time step of $\Delta t = \pi/8$ is insufficient to capture the physical process, but a time step of $\Delta t = \pi/16$ is sufficient. However, it is more likely to be stability which constrains model time step. In most practical ocean models, a wave (e.g. phase speed) is travelling across a discrete spatial grid. To ensure stability in models employing an explicit Euler scheme, the time step must be less than the time it takes for the wave to travel between adjacent grid points. This condition is known as the Courant-Friedrichs-Lewy (CFL) condition. For example, if the phase speed of a 1D tidal simulation, with grid spacing Δx, is $c = \sqrt{gh}$, then the model time step Δt must satisfy

$$\Delta t \leq \frac{\Delta x}{\sqrt{gh}} \tag{11.1}$$

For a typical shelf sea water depth $h = 50$ m, phase speed $c = 22.1$ m/s. Therefore, for a typical model structured grid spacing of $\Delta x = 200$ m, time step $\Delta t \leq 9$ s, i.e. considerably less than any constraint likely to be imposed by accuracy.

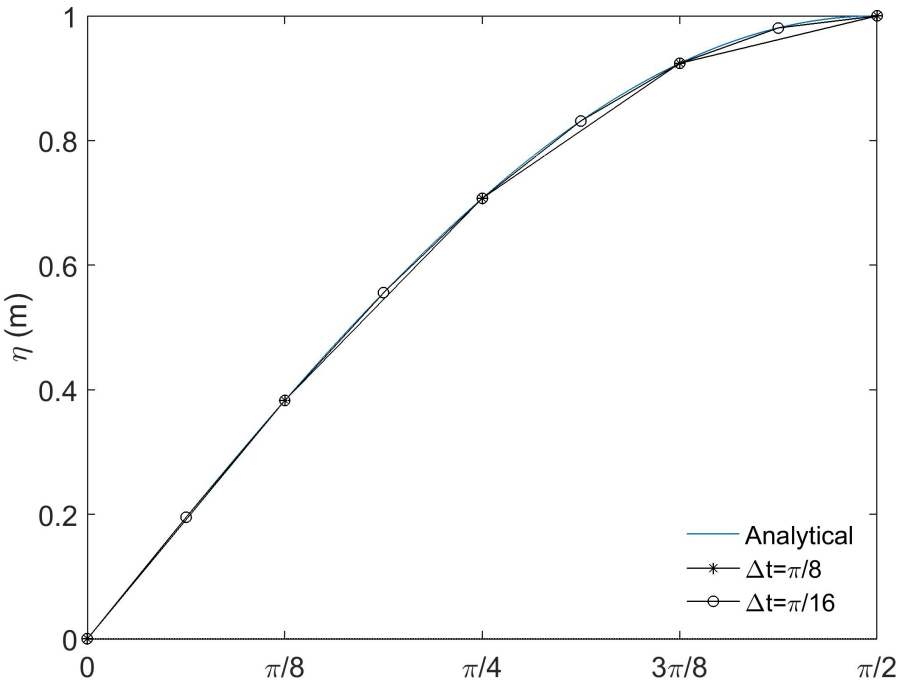

Figure 11.4: Influence of model time step (Δt) on accuracy.

Note that halving of the grid spacing requires a halving of the model time step (Eq. 11.1). However, for a 2D modelling problem, halving the grid (in both

x- and y-directions) results in a quadrupling of the number of computational grid points. Since the model time step is halved, the computational cost of the problem will have increased by a factor of eight! Both grid spacing and time step are therefore very important criteria when embarking on a model study. Local synchronisation of time integration in models with *unstructured* grids causes the time step to be constrained by the size of smallest mesh element, requiring careful mesh analysis and smoothing to avoid bottlenecks. By contrast, models such as SWAN [2] which employ *implicit* Euler time integration do not suffer from the same CFL-imposed restrictions.

11.2.2 Numerical Methods

Solution strategies for the differential equations underpinning wave and current models can be categorized into three main methods: finite difference, finite element and finite volume.

Finite differences have been used to approximate derivatives since the time of Leonhard Euler (1707-83). A *Finite Difference Method* converts differential equations into systems of linear algebraic equations which can be easily solved by matrix methods. The spatial and temporal domains are split into discrete and equally spaced points, and derivatives can be expressed in terms of differences between neighbouring values. For example, if the x-axis is discretized into points separated by Δx, a derivative of a function f can be approximated by $\frac{\partial f}{\partial x} \simeq \frac{f(x+\Delta x)-f(x)}{\Delta x}$ (the forward difference), by $\frac{\partial f}{\partial x} \simeq \frac{f(x)-f(x-\Delta x)}{\Delta x}$ (the backward difference), or by $\frac{\partial f}{\partial x} \simeq \frac{f(x+\Delta x)-f(x-\Delta x)}{2\Delta x}$ (the central difference, which is the mean of the forward and backward differences). It can easily be shown using Taylor series that the central difference more accurately approximates the derivative than the forward or backward differences. Finite difference schemes are used for structured grid calculations.

The *Finite Element Method* (FEM) is suitable for unstructured grid calculations and can therefore be used for irregular and complex geometries. A mesh of triangular (most common), quadrilateral or tetrahedral elements is generated, with higher resolution (i.e. smaller element size) in places of interest (such as near the coastline in Fig. 11.5). The solution to the system of partial differential equations is approximated by a series of basis functions, with the coefficients obtained by minimising an error function at the nodes of the grid.

The *Finite Volume Method* (FVM) is also based on an unstructured mesh. Rather than expressing conservation laws as partial differential equations, FVMs work with the integral forms. For instance, the differential form of the continuity equation can be written as,

$$\frac{\partial \rho}{\partial t} + \nabla.(\rho \mathbf{u}) = 0. \tag{11.2}$$

where $\mathbf{u}$ is the flow velocity and ρ is the density. Equation (11.2) can be integrated over any control volume (or a *finite volume*) V. Due to Stokes Theorem, the volume integral of the second term can be written as a surface integral over

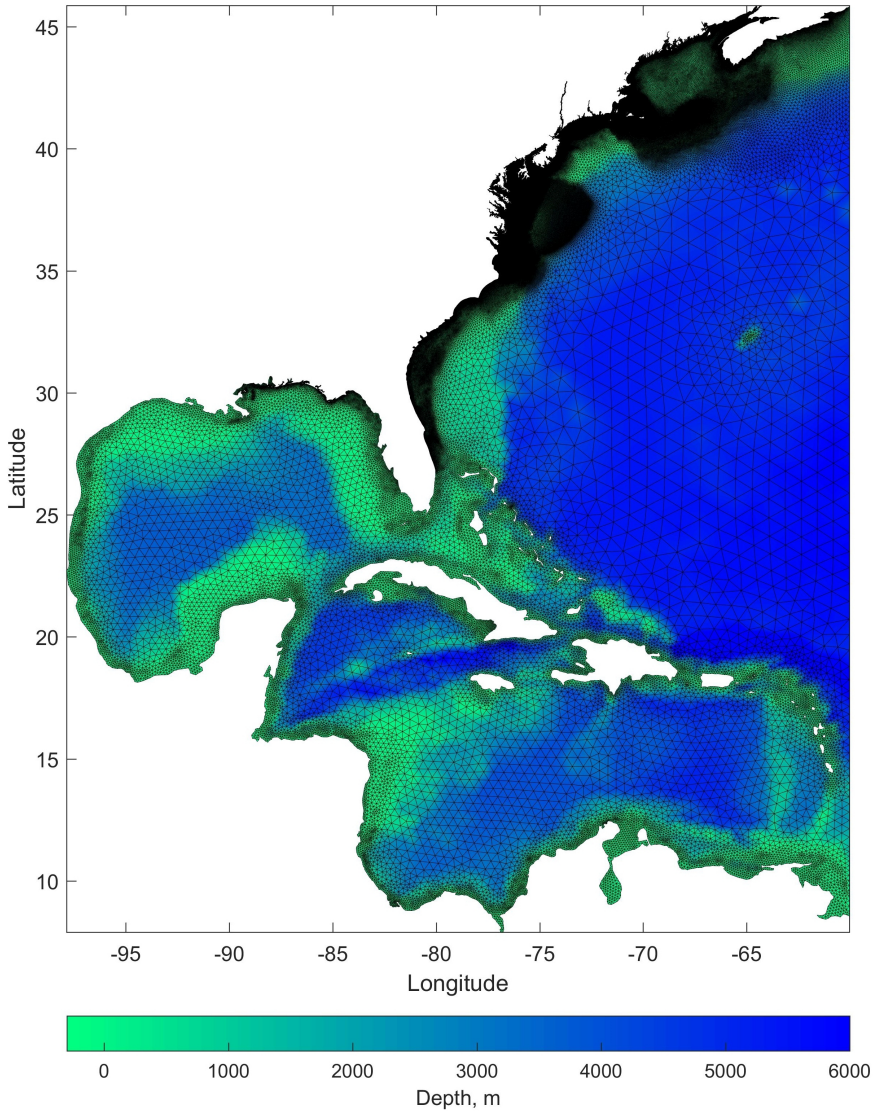

Figure 11.5: An example of a finite element triangular mesh used to simulate tides and storm surge over the northeast of the US. The mesh has 3,110,470 nodes and 6,114,065 elements, with a mean size of 333 m (10 m to ∼121 km) [10]

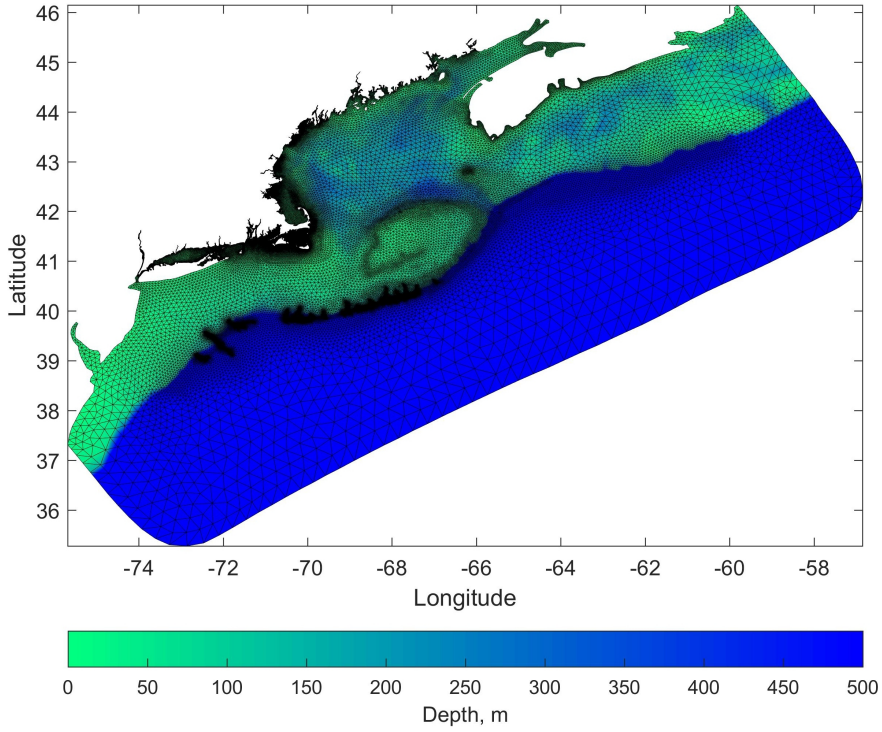

Figure 11.6: An example of a finite volume triangular mesh used to simulate tides and storm surge over the northeast of the US. This mesh is used by FVCOM (Finite Volume Coastal Ocean Model; [8]), for the Northeast Coastal Ocean Forecast System.

the volume's boundary ∂V, giving

$$\frac{\partial}{\partial t}\int_V \rho dV + \int_{\partial V} \rho \mathbf{u}.d\mathbf{S} = 0. \tag{11.3}$$

Therefore, the change of mass inside a control volume plus the net mass fluxes through the control surface should be zero. In FVM, the domain is first discretised into a number of non-overlapping finite volumes or cells (see Fig. 11.6 as an example). Usually, these "finite volumes" are triangles or prisms, depending on whether the model is two- or three-dimensional. Next, conservation laws are applied to each individual cell to form algebraic equations, which can be solved to compute the state variables. The use of integrals leads to more accuracy and stability, especially for sharp gradients (i.e. large derivatives) inside a domain, which is also called *shock-capturing* property.

11.2.3 Calibration and Validation

According to the statistician George Box, "all models are wrong, but some are useful". Models, however sophisticated, are a representation of reality. We need to evaluate and, if necessary, improve the fidelity of representation. *Calibration* is the process of tuning model parameters to maximise model accuracy. *Validation* is the process of measuring the accuracy of the final model. Both processes require representative in situ data from strategically positioned sensors.

Wave and current models must capture complex physical processes (such as friction, turbulent diffusion, and dissipation of wave energy by whitecapping, bottom interactions and depth-induced wavebreaking) within simplified, semi-empirical source terms. These include constants and coefficients (such as drag coefficient, eddy viscosity and bottom roughness) which may be chosen by the user. A process of calibration to choose suitable values for the free parameters can improve model fidelity. Repeated model runs are carried out for a range of (physically realistic) values of the parameter(s) in question to determine the model settings that produce the best agreement between the model prediction and measured sensor data at selected locations, as quantified by metrics which will be defined below.

To provide confidence in how closely a model output has simulated reality, it is necessary to perform validation with field data. Although it is often desirable for such data to be focussed in the region of interest, for example at the approximate location of a proposed wave or tidal energy array, this is not compulsory. If a model performs well in one region, or under one set of conditions (e.g. during a spring tide), this gives confidence in model performance in another region, or under another set of conditions (e.g. during a neap tide). To ensure the model has not been excessively tuned to fit data in one region or under one unique set of conditions, it is desirable for calibration and validation to use data from sensors at different locations if possible. Various metrics can be used to quantify model performance, and some of the most popular metrics are presented below.

Correlation coefficient

Correlation measures the direction and strength of the linear relationship between two variables. If we have a set of n observed (O_i) and simulated (S_i) values, the linear correlation coefficient (r) (also known as Pearson's r) can be calculated as

$$r = \frac{\sum_{i=1}^{n}(O_i - \overline{O})(S_i - \overline{S})}{\sqrt{\sum_{i=1}^{n}(O_i - \overline{O})}\sqrt{\sum_{i=1}^{n}(S_i - \overline{S})}} \tag{11.4}$$

For a perfect model, $r = 1$, while for a complete random prediction $r = 0$.

The square of the correlation is often used as a metric, since r^2 indicates the proportion of the variance in the observation that can be predicted by the model.

Root mean squared error (RMSE)

Root mean squared error (RMSE) is the square root of the mean of the square of all of the error. The use of RMSE is very common, and it is considered an excellent general purpose error metric for numerical predictions.

$$\text{RMSE} = \sqrt{\frac{1}{n}\sum_{i=1}^{n}(S_i - O_i)^2} \tag{11.5}$$

where O_i are the observations, S_i predicted values of a variable, and n the number of observations available for analysis. RMSE is a good measure of accuracy, but only to compare forecasting errors of different models or model configurations for a particular variable and not between variables, as it is scale-dependent

Scatter Index

Scatter index (S.I.) is simply the RMSE (Eq. 11.5) divided by the mean of the observations and multiplied by 100 to convert to a percentage error. This normalised quantity can be more easily interpreted than the raw RMSE. For example, if a RMSE for significant wave height is 1 m, this gives us no sense of how well the model is performing, since the mean of the observations could, for example, be either 1 m (S.I. = 100%) or 5 m (S.I. = 20%).

Bias

Bias (also known as mean error) is the mean of the simulated values of the selected variable minus the mean of the observed values, i.e.

$$BI = \overline{S} - \overline{O} \tag{11.6}$$

It is an index of the average component of the error [25], with a value closer to zero indicating a better simulation. A large mangnitude of bias indicates the presence of systemaic errors (for example, if there is insufficient dissipation due to whitecapping, then the model will over-predict significant waveheight.

11.3 Tidal Energy Resource Characterization

The International Electrotechnical Commission (IEC) has developed a technical specification for tidal energy resource assessment and characterization (IEC TS 62600-201). The main goal of IEC-62600-201 is to provide a uniform methodology, ensuring consistency and accuracy in the modelling, measurement, characterization, and analysis of the tidal stream resource, with the aim of accurately estimating Annual Energy Production (AEP) at locations suitable for the installation of an array of tidal energy devices [32]. IEC-62600-201 details the requirements for observations and modelling at two main stages of project development: Stage 1 (feasibility study) and Stage 2 (layout design study). In

Specification	Stage 1	Stage 2
Min. number of tidal constituents	4-8	8-12
Grid resolution at the area(s) of interest	500 m or 10 grid cells across a channel section	no more than twice turbine diameter
Model configuration	2D	3D
Tidal currents – Mobile survey	spring-tide survey at a minimum	spring- and neap-tide survey
Tidal currents – Stationary survey	35 day duration at a minimum	

Table 11.1: Overview of IEC-62600-201 recommendations for model and field surveys at different stages of project development.

general, for projects that exceed 10 MW (or 2% of the undisturbed resource), the requirements are as outlined in Table 11.1 for both stages of project development. In addition to these easily quantifiable metrics (e.g. minimum number of tidal constituents included in a model), there are less quantifiable requirements outlined in IEC-62600-21 for the Quality Control of bathymetry and tidal height data, meteorological data, turbulence, available wave data, and whether wave-current interaction should be accounted for, etc.

The mean AEP, in kWh, for each individual tidal energy device within an array can be estimated by combining the appropriate device power curve with either a time series of modelled or observed tidal resource data, or by using a probability distribution of the current velocity at the intended TEC deployment location. The mean annual energy production for the array can be estimated by summation of the individual device outputs.

11.3.1 Measuring the Tidal Resource

Up until the late 1980s, horizontal axis current meters were used to measure tidal currents. Although sometimes still in use today (since they are low cost and easy to deploy), the advent of the acoustic Doppler current profiler (ADCP) (Fig. 11.7) in the early 1990s revolutionised the way that currents are measured, particularly as they retrieve measurements of currents (in three dimensions) throughout the water column rather than at a single depth relative to either the sea bed or sea surface. This section considers ADCPs and related devices.

ADCP Theory

An ADCP is based on the Doppler effect, which is a familiar concept from the relative change in frequency of a car horn as it travels towards or away from an observer. If an observer is stationary while sound waves pass, n waves would

Figure 11.7: 4-beam (left) and 5-beam (right) acoustic Doppler current profilers (ADCPs).

pass during a time interval t. If the observer were to walk towards the source of sound, more than n waves would pass during t. Similarly, if the observer were to walk away from the source of sound, less than n waves would pass during t. The Doppler shift is the difference between the frequency heard while standing still, and the frequency heard when moving either towards or away from the sound. It is defined as

$$f_d = f_s(V/C) \tag{11.7}$$

where f_d is the Doppler shift, f_s is the frequency of sound when source and receiver are both stationary, V is the relative velocity between source and receiver, and C is the speed of sound, given by

$$C = f\lambda \tag{11.8}$$

where f is frequency and λ is wavelength.

An ADCP transmits sound at a fixed frequency, and listens to echoes returning from sound scatterers in a small volume of water, e.g. small particles or plankton that reflect the sound back to the instrument. Although the sound is scattered in all directions, a small amount is reflected back to the transducer. The ADCP is based on the assumption that these scatterers move at the same velocity as the water. Since the ADCP both transmits and receives sound, the Doppler shift is doubled, and so Eq. 11.7 becomes

$$f_d = 2f_s(V/C) \tag{11.9}$$

The Doppler shift only works with radial motion. Although angular motion changes the direction between source and receiver, it does not alter the distance

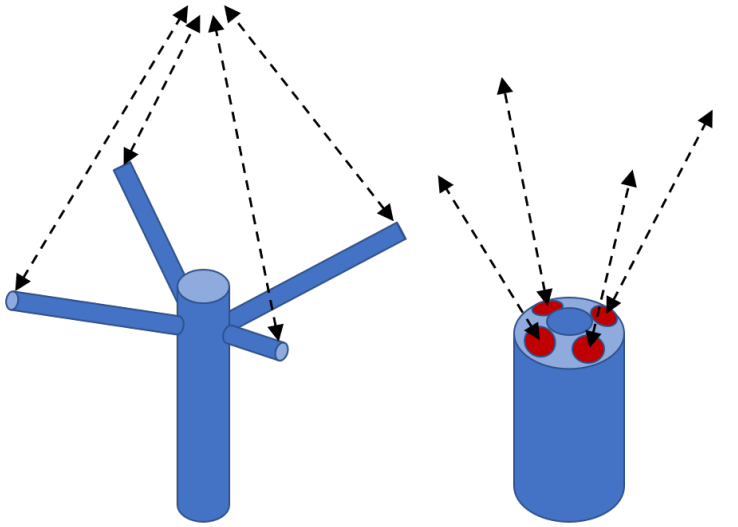

Figure 11.8: Beam configurations of (a) ADV (converging) and (b) ADCP (diverging).

separating them, and so does not cause a Doppler shift. Limiting the Doppler shift to the radial component, Eq. 11.9 becomes

$$f_d = 2f_s(V/C)\cos A \tag{11.10}$$

where A is the angle between the relative velocity vector and the line between the ADCP sensor and scatterers.

In contrast to an ADV (Acoustic Doppler Velocimeter) which has a *converging* beam pattern, an ADCP has a *diverging* beam pattern, and so by placing the ADCP on the sea bed looking upwards, the instrument can profile, under the correct frequency and configuration, the entire water column (Fig. 11.8).

An ADCP works on the assumption that there is horizontal homogeneity; otherwise the trigonometric relations that are used to calculate the velocity components are invalid. Since there are four beams, but only three current directions, one of the beams could be considered to be redundant. However, this fourth beam is used to measure the vertical velocity a second time, and the error between the two measurements gives an indication of the quality of the data (i.e. a measure of how valid the assumption of horizontal homogeneity has been).

The water column is partitioned into vertical *bins*. The ADCP listens to the reflected echos at different time intervals, which correspond to different distances from the transducer (since $v = d/t$), i.e. different bin depths. This process is known as *range gating* (Fig. 11.9). For example, if the time between the sent and

return signal is 8 ms, then the distance to the bin is 0.5×1500 m/s$\times 0.008$ s $= 6$ m (where 1500 m/s is the speed of sound in sea water, but clearly, in practice, an ADCP will use an accurate local value for the speed of sound, based on a local reading of water temperature and a constant value for salinity).

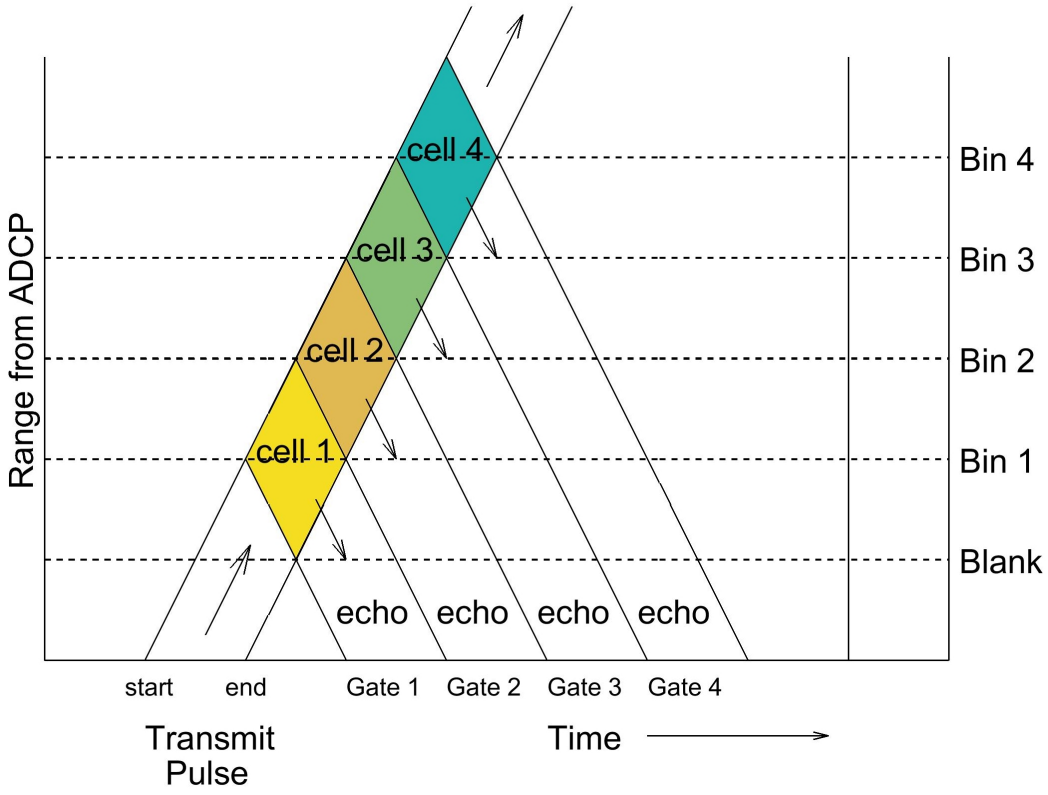

Figure 11.9: Range-time plot showing how ADCP transmit pulses and echos travel through space.

The echo from a hard surface such as the sea bed or sea surface is much stronger than the signal from scatterers in the water column, and so can dominate the signal. For this reason, data close to the surface (for an upward looking, moored, ADCP) or close to the bed (for a downward looking, hull-mounted, ADCP) is rejected. Also, since the ADCP will be at some height or depth in the water column, there will clearly be a further region of the water column which cannot physically be profiled. Further, the region close to the instrument is affected by *ringing* - an effect where the energy of a transmitted pulse lingers after the transmitted pulse has finished. Therefore, the ADCP must wait until the ringing has decayed before listening to and processing pulses. ADCPs are programmed with a default blanking period to eliminate measurements in this

zone (e.g. Table 11.2). Due to the blanking distance, physical height (or depth) of the instrument in the water column, and the echo from the surface (or bed), a significant portion of the water column is not sampled by an ADCP. Therefore, when post-processing, the velocity profile must be extrapolated into these regions of the water column, e.g. via curve fitting.

Frequency (kHz)	Maximum profile depth (m)	Ringing distance (m)
75	700	6
150	400	4
300	120	2
600	60	1
1200	25	0.5

Table 11.2: Nominal profiling range and ringing distance for a selection of RDI ADCPs [33].

To reduce errors from single ping (e.g. 2 Hz) velocity measurements, ADCP data are *ensemble averaged*. The averaging time period requires careful consideration. Larger averaging intervals will reduce uncertainty in the measurements, but at the expense of stationarity - the condition that properties of the flow such as the mean and the variance do not change significantly over the selected time period. For example, a one minute ensemble average would meet the condition of stationarity for most situations, but at the expense of relatively high instrument noise. A 10 minute averaging interval may reduce instrument noise to acceptable levels, but one must consider whether the flow is statistically 'stationary' over this time scale - this may not be the case if the flow is characterised by eddy shedding in the wake of an obstacle, for example.

ADCP Deployment

As noted in Table 11.1, a tidal current survey can either be mobile or stationary, the latter generally preferred during later stages of project development. During a mobile survey, the ADCP is either mounted into the hull of a vessel as a semi-permanent installation, or secured to the side of the vessel while the ship transects. The ADCP post-processing software will remove the ship's movement and other noise from the signal, but of course excessive movement (e.g. pitch and roll) will add to the uncertainty in the measurements. It is therefore important to only use mobile surveys during calm (wave) conditions and maintaining a low vessel speed, typically 2-3 knots. Of course mobile surveys have their limitations; since the tides are constantly evolving it is not possibly to simultaneously measure currents at all locations from a Lagrangian platform. However, mobile surveys can be useful for an initial site investigation, and when conducted correctly can be used to build up a spatial map of the tidal current distribution [e.g. 29].

In a stationary survey, the ADCP is mounted on the sea bed looking upwards, and generally remains in place for at least one lunar month (or a minimum

of 35 days as recommended in Table 11.1). The configuration shown in Fig. 11.10 is particularly suited to deployments where strong current speeds are anticipated, i.e. the majority of tidal energy sites, since the low profile 'trawl-resistant' instrument frame sits close to the sea bed, and hence within the near-bed boundary layer where the speed of the current is lower. If a non-trawl proof mooring is deployed in regions of strong tidal flow, the instrument frame should be sufficiently weighted to prevent post-deployment movement.

Acoustic Waves and Currents – AWAC

The ADCP shown on the right of Fig. 11.7 has five transducers, one of which is orientated vertically. Such an instrument, known as an AWAC (Acoustic Waves And Currents), can concurrently measure tidal currents and waves. It is therefore particularly useful, and cost effective, in studies where information on waves is required in addition to tidal data (for example, by IEC Technical Specification 62600-201). Section 11.4.1 contains a general description of wave measurement procedures, including a more detailed discussion on the role of AWACs.

11.3.2 Modelling the Tidal Resource

Table 11.1 shows the IEC Technical Specification 62600-201 minimum suggested model resolutions for various stages of project development. At stage 1 (feasibility study), the minimum resolution is of order 500 m, and so it is generally considered that a structured grid model will suffice (Section 11.2). However, at stage 2 (layout design study), where a minimum resolution of two turbine diameters is required to resolve the intra-device flows and device-device interaction, an unstructured grid model will almost certainly be required.

Hydrodynamic Modelling Software

As mentioned in Section 11.2, partly linked to model grid type (structured versus unstructured), is the model formulation – either finite difference, finite element, or finite volume. There is a vast array of modelling software used for tidal resource characterization, and so here we focus on an example of each type, with reference to published studies. However, one important consideration is whether model code is commercial or open source. This also applies to software that is used for model pre- and post-processing, since a license for commercial software such as Matlab could be prohibitively expensive for a small organization, when open source alternatives such as Python exist.

Finite difference case study – ROMS

Orkney is an archipelago in the north of Scotland, separated from the Scottish mainland by the 12 km width of the Pentland Firth. Orkney is comprised of around 70 islands, separated by a series of bays and energetic tidal channels (Fig. 11.11). Orkney is mesotidal; however, tidal waves in the region, dominated by

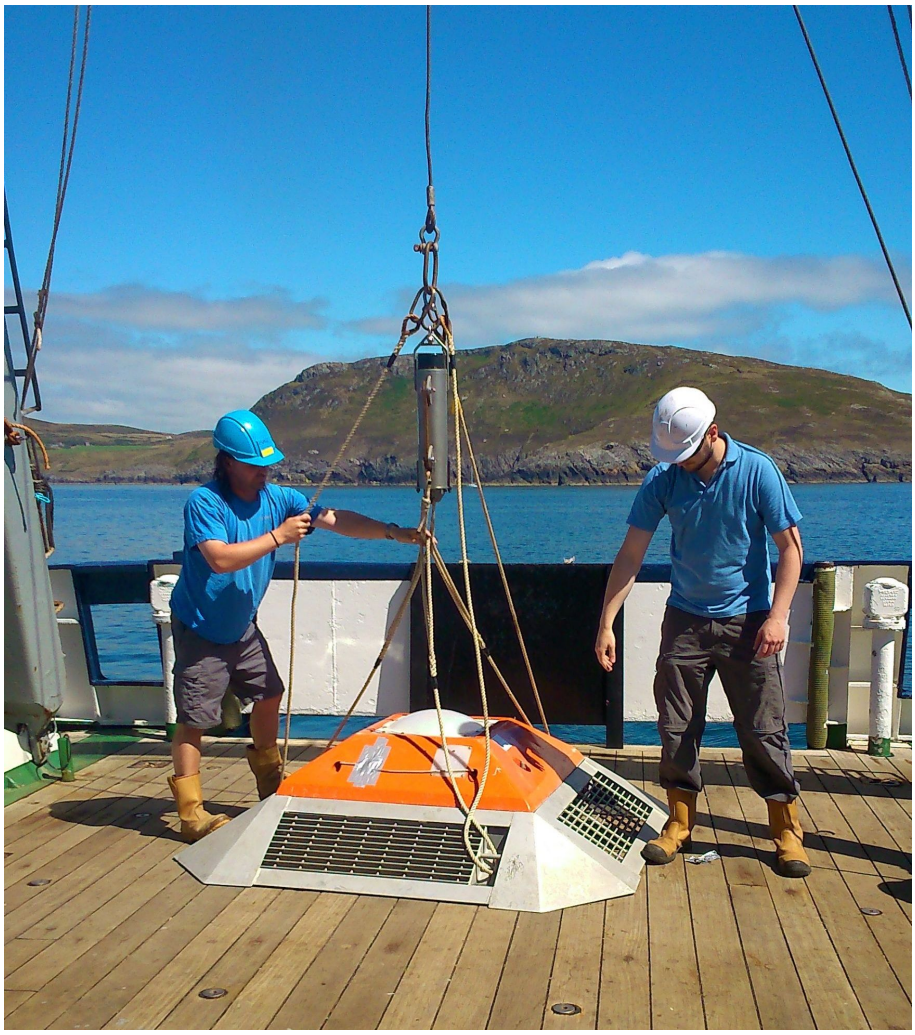

Figure 11.10: Low profile ('trawl-resistant') ADCP mooring. The acoustic release above the instrument is used during the deployment stage; a similar acoustic release, in the base of the instrument frame, is used during recovery. The orange part of the instrument, which is buoyant, separates from the heavy base when the (recovery) acoustic release is triggered. The top and bottom parts of the mooring are connected by a cable, which is coiled inside the base prior to deployment.

the principal semidiurnal lunar (M_2) and solar (S_2) constituents, take around two and a half hours to propagate around Orkney from the western to the eastern approaches of the Pentland Firth, leading to a considerable phase lag across Orkney [27]. This phase lag results in a strong pressure gradient across Orkney, driving strong tidal flows through the Pentland Firth and along the Firths of Orkney. Between Westray Firth and Stronsay Firth is the Fall of Warness, where the EMEC grid connected tidal test site is situated.

ROMS model

To examine the tidal energy resource of Orkney, the finite difference structured grid 3D ROMS (regional ocean modelling system) model was applied. ROMS simulates tidal hydrodynamics using a finite-difference approximation of the 3D RANS (Reynolds-averaged Navier-Stokes) equations with hydrostatic and Boussinesq assumptions, and a split-explicit time stepping algorithm, on a horizontal curvilinear Arakawa-C grid and terrain-following vertical coordinate system [36].

The primitive momentum balance in the x and y directions (Cartesian coordinates) are described by

$$\frac{\partial u}{\partial t} + \vec{v} \cdot \nabla u - fv = -\frac{\partial \phi}{\partial x} - \frac{\partial}{\partial z}\left(\overline{u'w'} - \nu \frac{\partial u}{\partial z}\right) + \mathcal{F}_u + \mathcal{D}_u \tag{11.11}$$

and

$$\frac{\partial v}{\partial t} + \vec{v} \cdot \nabla v + fu = -\frac{\partial \phi}{\partial y} - \frac{\partial}{\partial z}\left(\overline{v'w'} - \nu \frac{\partial v}{\partial z}\right) + \mathcal{F}_v + \mathcal{D}_v \tag{11.12}$$

where u, v, w are the x, y, z components of vector velocity $\vec{v}$, f is the Coriolis parameter, ν the molecular viscosity, $\mathcal{F}$ and $\mathcal{D}$ denote the forcing and diffusive terms, respectively, with the subscript giving the direction. An overbar indicates a time average, and a prime ($'$) indicates a fluctuating turbulent quantity, ϕ is the dynamic pressure term, and g is acceleration due to gravity.

In the Boussinesq approximation, density variations are neglected in the momentum equations except in their contribution to the buoyancy force in the vertical momentum equation. Under the hydrostatic approximation, it is further assumed that the vertical pressure gradient balances the buoyancy force:

$$\frac{\partial \phi}{\partial z} = -\frac{\rho g}{\rho_o} \tag{11.13}$$

Finally the continuity equation for an incompressible fluid is applied:

$$\frac{\partial u}{\partial x} + \frac{\partial v}{\partial y} + \frac{\partial w}{\partial z} = 0 \tag{11.14}$$

Model setup

Since ROMS is formulated on a regular (curvilinear) finite difference grid, it was necessary to nest a model of Orkney to obtain the necessary resolution. To provide boundary conditions for the higher resolution nested Orkney model, it was

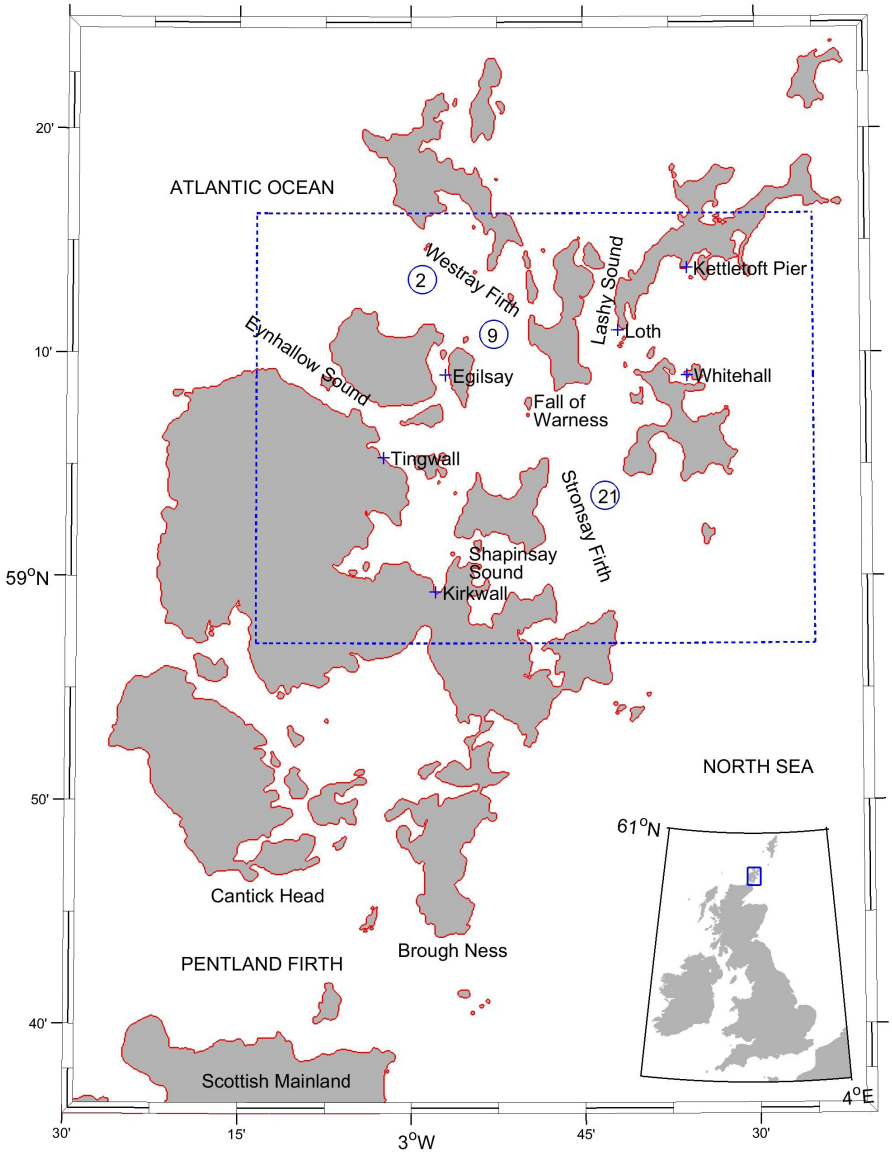

Figure 11.11: Principal locations in Orkney and surrounding waters. The dashed box shows the boundaries of the high resolution nested model, and tide gauge stations used for model validation (labelled) are shown as blue crosses. Numbered circles are locations where time series are presented in the results section. Inset shows the location of Orkney in relation to the British Isles. Figure adapted from Neill et al. [27].

necessary to first run a north of Scotland regional model at coarser resolution. The regional model extended from 4°30′W to 0°30′W, and from 58°18′N to 60°03′N, encompassing the Pentland Firth, Orkney, and part of Shetland (Fig. 11.12). The regional model had a horizontal grid spacing of $1/120 \times 1/228°$ (approximately 500 m × 500 m), and was forced at the boundaries by FES2012 (1/16° resolution) currents and elevations for the M_2 and S_2 constituents [7]. Bathymetry for the regional model was interpolated from 1/120° GEBCO data. The regional model was run with 10 equally distributed vertical (sigma) levels for a period of 15 days, and tidal analysis of the elevations and depth-averaged velocities used to generate astronomical boundary forcing for the inner nested high resolution Orkney model.

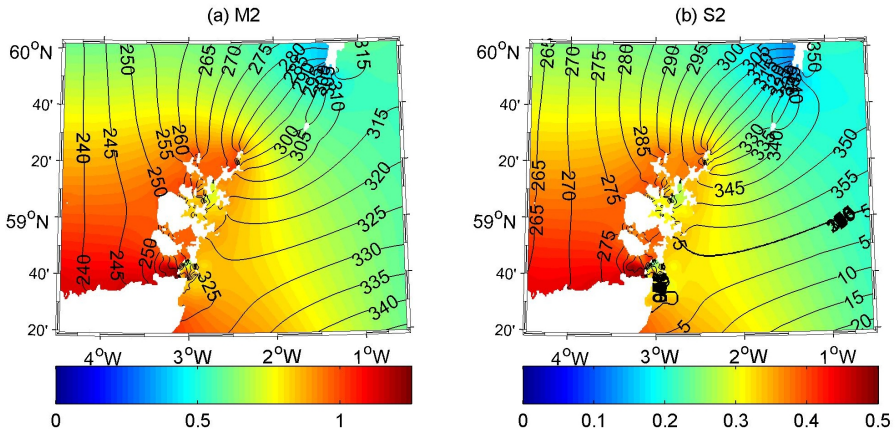

Figure 11.12: M_2 and S_2 co-tidal charts calculated from the north of Scotland regional ROMS model. Colour scale is amplitude (m), and contours are phase (degrees relative to Greenwich).

The high resolution Orkney model extended from 3°13.5′W to 2°25′W and from 58°57′N to 59°16′N at a grid resolution of $1/750 \times 1/1451°$ (approximately 75 m × 75 m) (the dashed box shown on Fig. 11.11). Bathymetry was interpolated from relatively high resolution (approximately 200 m) gridded multibeam data provided by St. Andrew's University. The model domain encompasses the principal high tidal flow regions of Orkney, including Westray Firth and Stronsay Firth, and the EMEC tidal test site at the Fall of Warness. The model configuration used the GLS turbulence model, tuned to represent the $k-\varepsilon$ model, and included horizontal harmonic mixing to provide sub-grid scale dissipation of momentum [41], and quadratic bottom friction, with a drag coefficient $C_D = 0.003$. This value for the drag coefficient is consistent with previous ROMS studies which simulate the flow through energetic tidal channels, and these studies have demonstrated that the ROMS model is not particularly sensitive to the value of C_D [39, 37]. The model was again run with 10 vertical levels for a period of 15 days.

Table 11.3: ROMS modelled amplitude H (m) and phase g (degrees relative to Greenwich) compared with values at tidal stations around Orkney for M_2 and S_2 constituents. Locations of tidal stations are shown in Fig. 11.11. Observations were obtained from Admiralty Tide Tables.

Station	M_2				S_2			
	Observed		Modelled		Observed		Modelled	
	H	g	H	g	H	g	H	g
Kirkwall	0.84	301	0.87	297	0.29	339	0.31	327
Egilsay	0.88	282	0.86	287	0.32	316	0.31	316
Whitehall	0.88	310	0.92	313	0.31	345	0.34	344
Loth	0.74	300	0.78	302	0.26	336	0.28	333
Kettletoft Pier	0.92	312	0.92	313	0.33	347	0.34	344
Tingwall	0.86	276	0.85	286	0.31	310	0.31	315

Model validation

To validate the model, we made use of the harmonic constants published in Admiralty Tide Tables, which are based on harmonic analysis of observations which have a minimum record length of one month. The regional model was validated at 14 tide gauge stations throughout the region, with a root-mean-square-error (RMSE) in amplitude of 8.3 cm for M_2, and 3.7 cm for S_2, based on harmonic analysis of the 15 days of model simulation – a sufficient record length to separate the M_2 and S_2 constituents. The corresponding RMSE in phase was 6.8° and 7.5° for the M_2 and S_2 tidal constituents, respectively. We present the validation of the high resolution Orkney model in more detail (Table 11.3). For the high resolution model, the RMSE in amplitude for the 6 available tide gauge stations was 2.7 cm for M_2, and 1.7 cm for S_2, again based on harmonic analysis of the 15 day model simulation. The RMSE in phase was 5.0° and 5.5° for the M_2 and S_2 tidal constituents, respectively.

Results

The peak depth-averaged tidal currents and the corresponding peak velocity vectors are shown in Fig. 11.13. Clearly, tidal flow is strongest at the constrictions of narrow channels (e.g. Lashy Sound, Eynhallow Sound and, in particular, the Fall of Warness – see Fig. 11.11 for locations). The peak current speed reaches 3.7 m s^{-1} (7 knots) in Lashy Sound and the Fall of Warness, and since the model was forced with the two principal semi-diurnal tidal constituents, M_2 and S_2, these represent peak spring tidal currents.

Time series of the depth-averaged and depth-varying tidal currents show that there are large variations in tidal asymmetry along the Westray and Stronsay Firths (Fig. 11.14). We show results for three locations which exhibit varying degrees of asymmetry: site 2 (ebb-dominant), site 9 (symmetrical), and site 21 (flood-dominant) (locations are shown on Fig. 11.11). Above the boundary

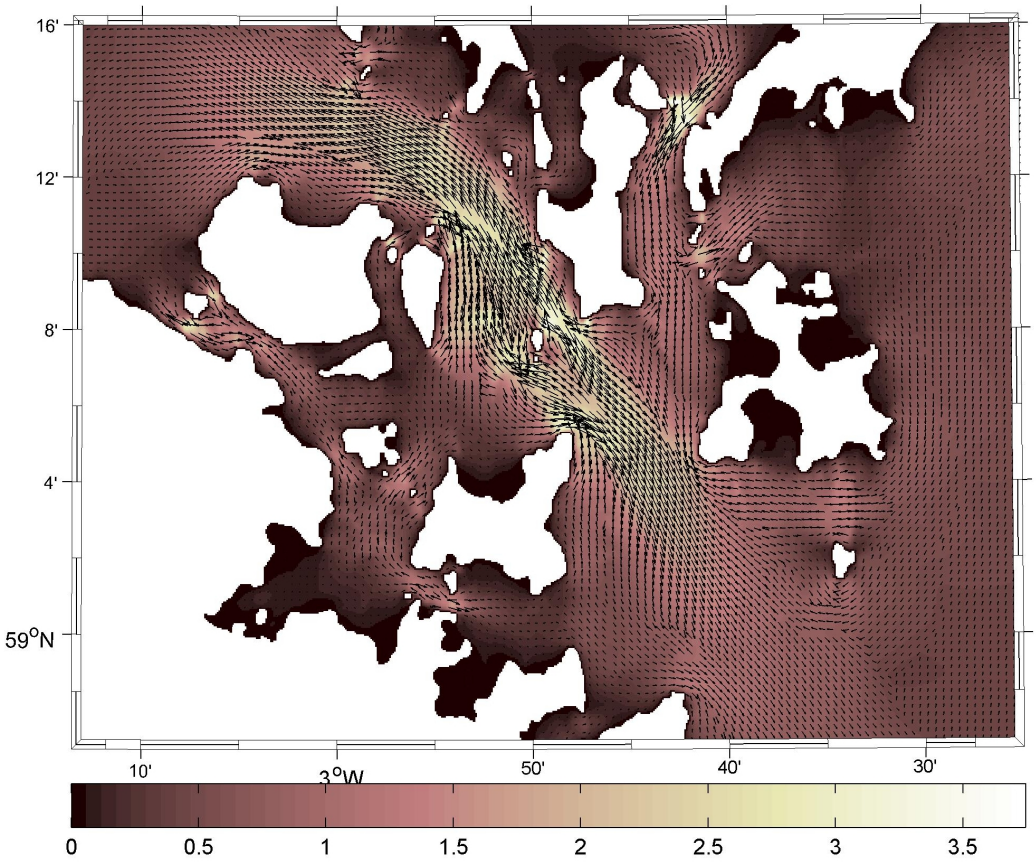

Figure 11.13: Peak current speed (colour scale) and the associated peak spring velocity vectors. For clarity, only every 5th vector in both zonal and meridional directions has been plotted.

layer, the asymmetry at sites 2 and 21 is evident at all depths in the water column, and is more pronounced during spring tides. Therefore, for all practical scenarios of energy extraction, i.e. device hub placed at some height in the water column that is above the near-bed boundary layer and in regions of low velocity shear, strong velocity asymmetry will translate into an even stronger asymmetry in power output (since power is related to velocity cubed). Such asymmetry in the flow field is clearly undesirable from an electricity generation perspective, and so symmetrical sites (such as site 9) are more attractive for commercial development.

Finite element case study – TELEMAC

To complement the structured grid application described in the previous section, we here present an unstructured (finite element) case study using TELEMAC-2D that includes energy extraction. This is based on a paper published by Robins et al. [35] that primarily investigates the environmental impact of energy extraction in the Anglesey Skerries (Irish Sea), but also quantifies the resource of the region.

TELEMAC model

TELEMAC-2D uses the finite element method, applied to a computational mesh composed of triangular elements, to solve the Saint-Venant equations of continuity

$$\frac{\partial h}{\partial t} + \vec{u} \cdot \nabla h + h \nabla \cdot \vec{u} = S_h \tag{11.15}$$

x-momentum

$$\frac{\partial u}{\partial t} + \vec{u} \cdot \nabla u = -g \frac{\partial Z}{\partial x} + S_x + \frac{1}{h} \nabla \cdot (h \nu_t \nabla u) \tag{11.16}$$

and y-momentum

$$\frac{\partial v}{\partial t} + \vec{u} \cdot \nabla v = -g \frac{\partial Z}{\partial y} + S_y + \frac{1}{h} \nabla \cdot (h \nu_t \nabla v) \tag{11.17}$$

where h is water depth, u, v are components of the depth-averaged velocity $\vec{u}$, Z is the free surface elevation, ν_t is momentum diffusion, S_h is source or sink of fluid, and S_x and S_y are source terms in the dynamic equations that account for wind, Coriolis force, bottom friction, and a source or sink of momentum.

To simulate tidal stream energy extraction, we introduced an additional drag force in the eastward and northward directions, F_x and F_y, respectively, at the locations (nodes) of energy extraction as follows:

$$F_x = -C_p \frac{P}{\rho A U h} \cos(\theta) \tag{11.18}$$

$$F_y = -C_p \frac{P}{\rho A U h} \sin(\theta) \tag{11.19}$$

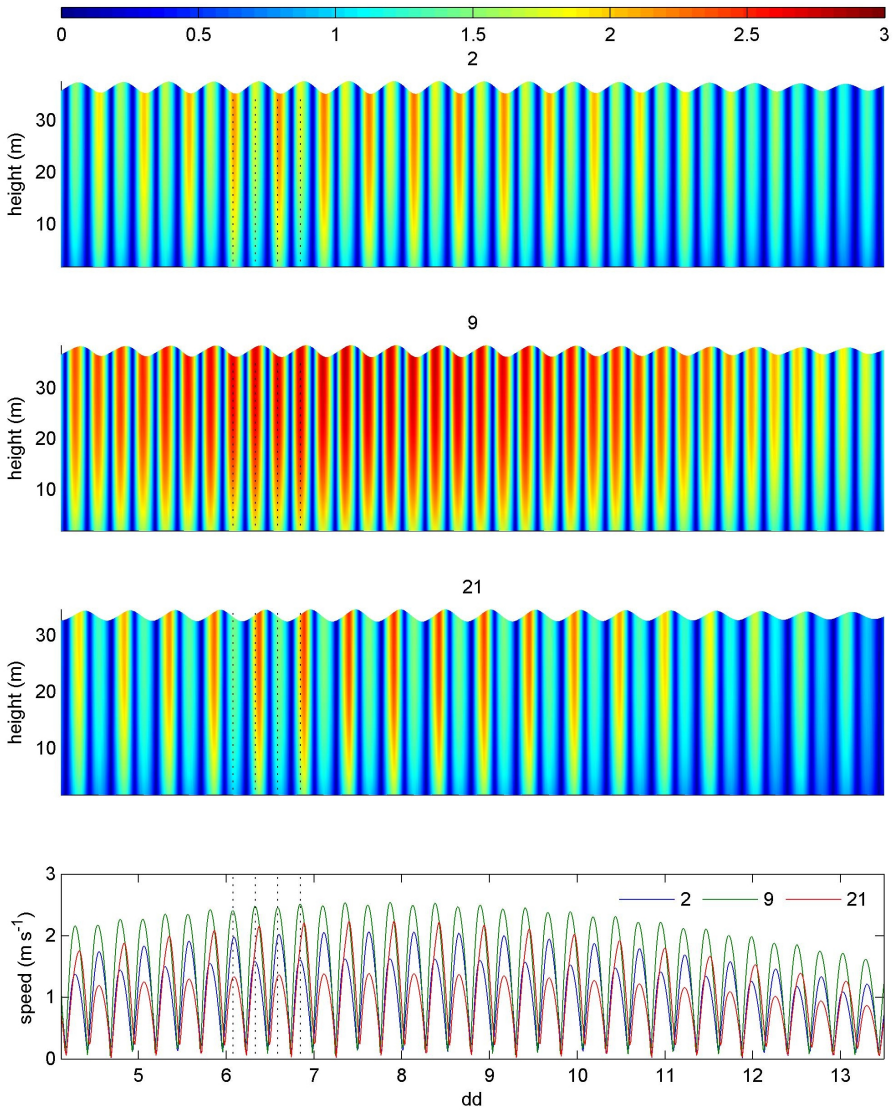

Figure 11.14: Time series of simulated current speed in January 2000 at three contrasting sites: site 2 (ebb-dominant), site 9 (almost symmetrical), and site 21 (flood-dominant). The lower panel shows a time series of depth-averaged current speed. For reference, vertical dashed lines are located at peak flood and ebb conditions for site 9.

where ρ is the water density, A is the 'plan' area of seabed which each individual turbine affects, and θ is the direction of the depth-averaged current, U. We assumed a typical power curve [28] to parameterize extracted power, P for each turbine, with a cut-in velocity of 0.7 m/s and rated velocity of 2.7 m/s, which produced 2 MW (assuming two drivetrains per device). We assumed a constant power coefficient (C_p) at the location of extraction of 0.35. Support structure (drag) losses have been assumed negligible.

Model setup

The advantage of an unstructured (triangular) mesh is that it can accommodate considerable changes in grid resolution within a single computational domain. It is therefore possible to incorporate processes from the edge of the continental shelf seas through to array scale without resort to nesting.

An unstructured model mesh of the Irish Sea was developed using BlueKenue grid generation software, with 2000 m at the offshore boundaries, increasing to 200-500 m in coastal areas, and 15-50 m around northwest Anglesey and in the region of the tidal energy array (Fig. 11.15). The computational mesh was mapped onto gridded Admiralty bathymetry data available at 200 m resolution.

Model validation

Prior to array operation, a baseline simulation was implemented to validate the model. This simulation was forced by the principal semi-diurnal lunar (M2) and solar (S2) tidal constituents and, following a 24 h model spin-up, run for a period of two spring-neap tidal cycles (i.e. 29.5 days) which was of sufficient length to diminish any artifacts due to model spin-up. The modelled hydrodynamics were validated throughout the Irish Sea, against known tide gauge measurements, giving root mean square errors in M2 amplitude and phase of 10 cm and 7°, respectively, which is comparable with other (3D) models of the region [e.g. 34].

Results

Typical time series of velocity and power output is shown in Fig. 11.16 noting that, due to the device power curve, the power peaks at 1200 kW when the current speed equals or exceeds the rated velocity of the device (2.7 m/s). By extending the model output to one year, the Annual Energy Production (AEP) (assuming 100% availability) is 3423 MWh, corresponding to a respectable capacity factor of 32.7%.

11.4 Wave Energy Resource Characterisation

11.4.1 Measuring the Wave Resource

Validation of numerical wave models requires in situ sensors to produce an accurate, unbiased and complete set of measurements including significant wave

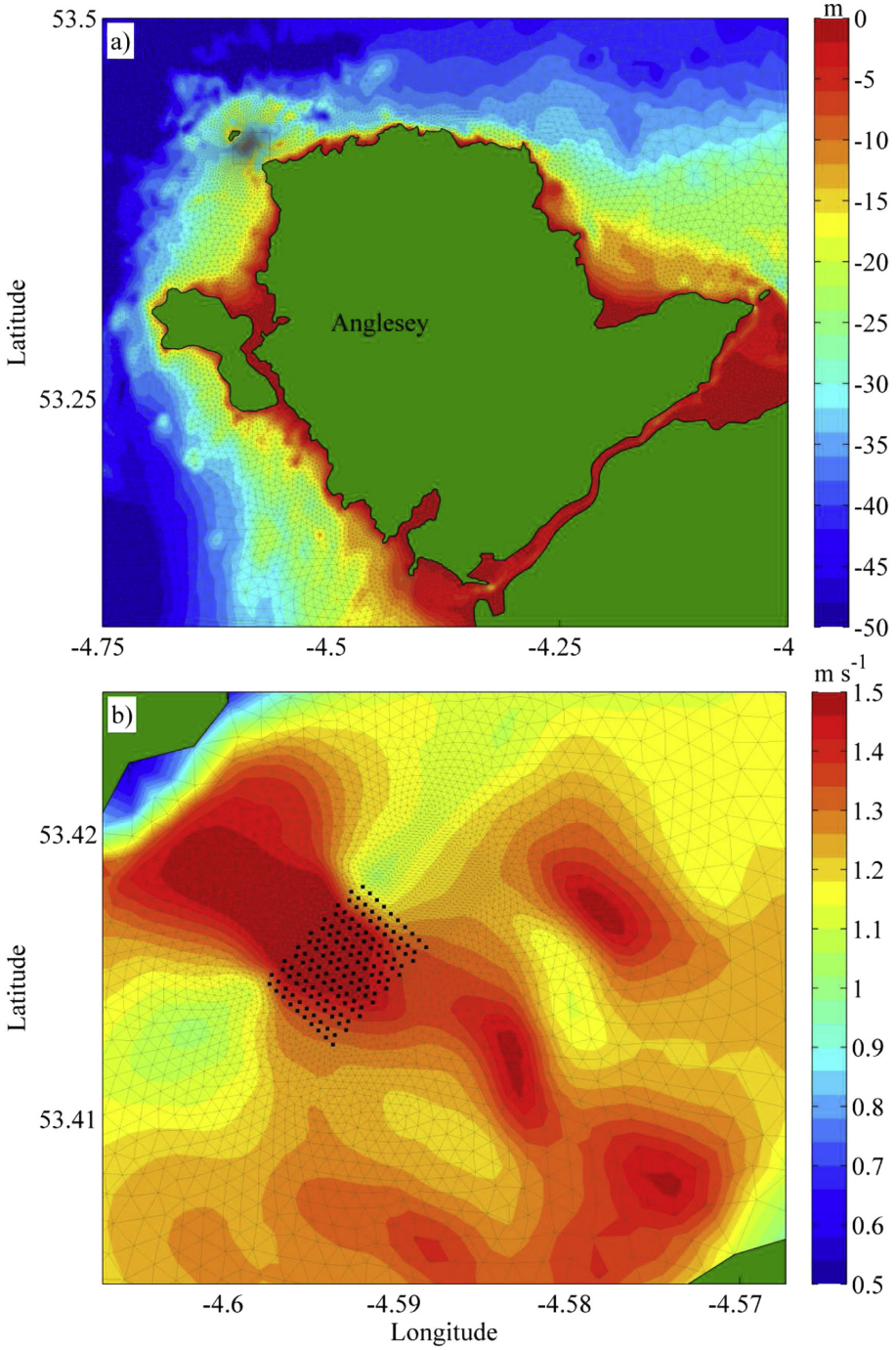

Figure 11.15: Sub-sections of the Irish Sea Model grid: (a) Anglesey and (b) the Skerries Channel. Colour contours in (a) denote water depth at mean sea level (m), and (b) mean depth-averaged velocities (m/s). The finite-element grid has variable resolution and edge lengths which connect nodes where parameters are calculated. The region of the tidal energy array in the Skerries Channel is shown in (b) – the location chosen based on both bathymetry and velocities; each highlighted (black) node represents one turbine (i.e. 2 MW of extractable power) where tidal energy extraction takes place. In the figure, 150 highlighted nodes represent a rated capacity array of 300 MW which, for our array configuration, generated a mean of 141 MW over a spring-neap cycle. Reproduced from [35] under open source license.

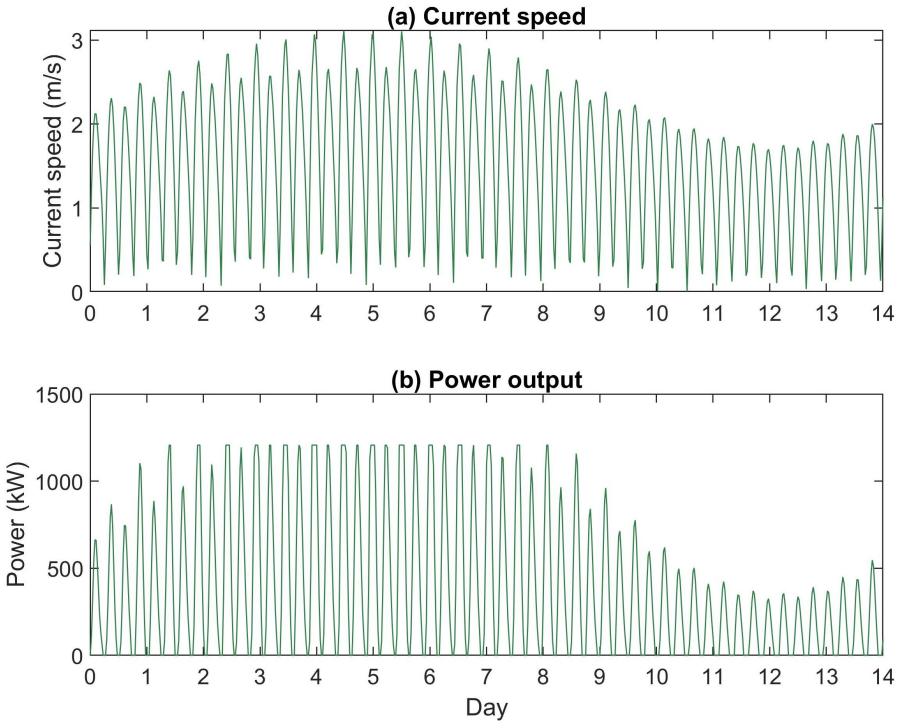

Figure 11.16: Simulated (a) current speed, and (b) power output for 1200 kW Seagen device at Anglesey Skerries over a 14 day period.

height, energy period and omnidirectional wave power. Certain classes of resource assessment also require spectral width and directional spreading index. Wave measurements can also be used for calibration, or as boundary conditions for local models. Furthermore, wave measurements offer additional insights into the wave regime which can be invaluable for site characterization. Observations include extrema as well as non-linear effects that are parametrised within wave models (e.g. wave-wave interactions), and processes that are difficult and computationally expensive to simulate, e.g. interaction between wave and tidal resources.

Waves exhibit considerable seasonal and interannual variability. To capture a full range of conditions (avoiding seasonal bias), one should deploy a sensor which can provide hourly measurements (such as a buoy) for a full year, or a sensor with a lower sample frequency (e.g. daily) for longer.

To recreate the conditions at a particular wave energy site, it would be ideal to deploy a sensor as close as possible to the proposed site itself. Alternatively, a deployment location should have a wave climate representative of typical conditions at the area of interest, and a similar water depth. Locations with rapid spatial variation in wave climate, such as near islands or large bathymetric features are best avoided, as is deployment in the surfzone. Building in redundancy by deploying multiple sensors offers mitigation against damage or loss, as well as providing a richer choice of data for validation, calibration and direct characterization.

In the remainder of this section, we will consider three main types of sensor: surface following buoys, bottom mounted acoustic wave sensors and remote sensors.

Surface Following Buoys

Surface-following wave measuring buoys have been ubiquitous for decades, with networks of permanent moorings such as Wavenet in the UK (see Figure 11.1) offering datasets extending back many years, as well as numerous short-term deployments. *Heave-pitch-roll* buoys follow and measure the surface slope: the vertical (heave) displacement data, used for the omnidirectional spectrum and associated moments, is supplemented by directional information obtained by the buoy's angles of orientation with respect to the horizontal axes. In contrast, *particle-following* buoys (such as the series of Datawell Waverider buoys, an example of which is pictured in Figure 11.17) follow the motion of the water particles at the surface, and the sensors sit within a stabilised platform designed to remain horizontal rather than tilting with the wave surface. Again, the vertical displacement data is used for the waveheight spectrum, with directional information provided by lateral motion along the horizontal axes. The most common particle-following buoys contain a vertical and two horizontal accelerometers. Displacements are obtained through double integration, which is achieved by convoluting the acceleration signals with a numerical filter. The signature of this filter may occasionally appear in the displacement data if the buoy experiences a large, sharp, impulse-type acceleration. Some, more recent

Figure 11.17: A Datawell Waverider surface following buoy ready for deployment to the west of Anglesey, Irish Sea, by Bangor University (Photograph: S. Ward)

buoys use GPS-type positioning to measure velocity and hence displacement in the three orthogonal directions. Data can be sent to shore in almost real time by HF signal, mobile internet/SMS or satellite communication (for remoter areas) or else read from an internal memory card on recovery.

An omni-directional power spectrum $P(f)$ is obtained by Fast Fourier Transform (FFT) from the heave signal. The most common Datawell Waverider-MkIII measures displacements at a sample rate of 1.28Hz, and produces spectra in the range from 0.025Hz to 0.58Hz. The lower bound of the frequency range is determined by the duration of the sample window for the FFT while the upper bound results from the wavelength starting to approach the physical dimensions of the buoy, as well as the sampling frequency. By taking the moments of these spectra, the buoy also reports timeseries of spectral parameters such as significant waveheight and mean wave period. Further parameters can be obtained by taking ratios of the moments provided. For example, the energy period $T_{-1,0}$ can be obtained by squaring $T_{-1,1}$ and dividing by $T_{0,1}$ (or by directly integrating the spectra). Upcross parameters such as maximum wave height derived from the displacement timeseries are also reported.

The remaining sensors (horizontal displacements or pitch and roll data) provide directional information about the directional spectrum $S(f,\theta)$, which is defined as

$$S(f,\theta) = P(f)D(\theta|f), \tag{11.20}$$

where $D(\theta|f)$ is the spreading function at a given frequency. This spreading function is periodic in wave direction θ, is normalised so that

$$\int_{-\pi}^{\pi} D(\theta|f)\mathrm{d}\theta = 1, \tag{11.21}$$

and has the Fourier decomposition

$$\pi D(\theta|f) = \frac{1}{2} + \sum_{n=1}^{\infty} \left[a_n(f)\cos n\theta + b_n(f)\sin n\theta\right], \tag{11.22}$$

in terms of the "directional moments" for each frequency $a_n(f)$ and $b_n(f)$ which can therefore be obtained by integration of the spreading function:

$$a_n(f) = \int_{-\pi}^{\pi} D(\theta|f)\cos n\theta\mathrm{d}\theta, \quad b_n(f) = \int_{-\pi}^{\pi} D(\theta|f)\sin n\theta\mathrm{d}\theta. \tag{11.23}$$

The first two pairs of these moments (11.23) for each frequency bin (we shall henceforth drop the explicit frequency dependence) can be obtained from the buoy's co- and quad-spectra arising from its horizontal displacements. The $n = 1$ pair gives the mean wave direction

$$\theta_0 = \mathrm{atan2}(b_1, a_1) \tag{11.24}$$

and hence the *centred moments* m_n and n_n for $n = 1, 2$:

$$\begin{bmatrix} m_n \\ n_n \end{bmatrix} \equiv \begin{bmatrix} \cos(n\theta_0) & \sin(n\theta_0) \\ -\sin(n\theta_0) & \cos(n\theta_0) \end{bmatrix} \begin{bmatrix} a_n \\ b_n \end{bmatrix} = \begin{bmatrix} \int_{-\pi}^{\pi} D(\theta|f)\cos n(\theta-\theta_0)\mathrm{d}\theta \\ \int_{-\pi}^{\pi} D(\theta|f)\sin n(\theta-\theta_0)\mathrm{d}\theta \end{bmatrix}. \tag{11.25}$$

There are three such moments (since (11.24) and (11.25) give $n_1 = 0$). Together with the mean wave direction θ_0 and the $n = 0$ moment of the *un*-normalised spreading function (i.e. the omnidirectional power spectrum density at a given frequency), these are known as the "first five" moments for each frequency bin. The directional moments can also be presented as spread σ, skew γ and kurtosis δ defined as

$$\sigma = \sqrt{2(1 - m_1)}, \quad \gamma = -\frac{n_2}{\sigma_2^3}, \quad \delta = \frac{6 - 8m_1 + 2m_2}{\sigma_2^4}, \tag{11.26}$$

where σ is expressed in radians. It can be shown [22] that this is the maximum amount of information which can be directly obtained from a single-point sensor such as a wave buoy. To obtain a unique directional spectrum from the set of directional moments requires a further constraint, since infinitely many possible spreading functions $D(\theta|f)$ could satisfy (11.23).

The *principle of maximum entropy* states that the probability distribution (i.e. $D(\theta|f)$) which best represents the current state of knowledge (i.e. the measured set of moments) is the one with the largest *entropy*, which can be defined for directional data as

$$H = -\int_{-\pi}^{\pi} D(\theta|f) \ln D(\theta|f) \mathrm{d}\theta. \tag{11.27}$$

Numerical tools which construct maximum entropy spectra from buoy data are available [6, 9], using Newtonian iteration procedures which build on an analysis presented by [15]. Figure 11.18 shows some of the different types of data available from a Datawell Waverider MkIII buoy, deployed in at the UK Wave Hub test site. The data was recorded during the largest storm of 2016, on the 8th of February: the significant waveheight for the time period in the plots was 10.03m. The half-hourly data is plotted as displacements, and omnidirectional and directional spectra.

Acoustic Wave Sensors

The operation of acoustic Doppler velocity sensors, and their role in tidal energy reosurce characterisation, was described in 11.3.1. Wave measuring capability can also be incorporated into bottom mounted acoustic sensors, such as the AWAC (Acoustic Waves And Currents). An additional, vertical Acoustic Surface Tracking beam uses echo-ranging to measure the vertical surface displacement, which can be processed into omnidirectional spectra. A pressure sensor provides another source of heave data. The four diverging beams (used to measure flow information when the device is operating as a current sensor) capture the orbital velocities and hence provide directional information. The Maximum Likelihood Method is used to calculate a directional spectrum from this data.

An AWAC can be deployed at a wide range of water depths: accurate measurements over a range of frequencies can be obtained for depths between 10m and 100m (or deeper, if mounted on a subsurface buoy). It is less susceptible

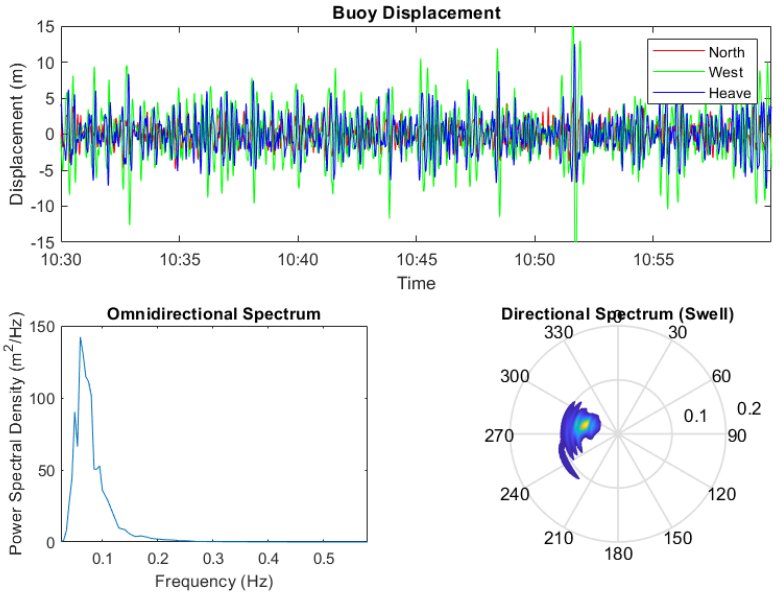

Figure 11.18: Wave displacements and spectra measured by a Datawell Waverider Mk III buoy at the UK Wave Hub test site (50.35° N, 5.61° W) during a storm on the 8th Februrary 2016. For the half-hour recording period from 10:30am, the significant wave height was 10.12m, the maximum wave height was 19.14m and the peak period was 16.7s. The displacements and omnidirectional spectrum were calculated by the buoy software and the directional spectrum (plotted for the swell only) using [9]. Data courtesy of the Southwest Regional Coastal Monitoring Programme, distributed under the UK Open Government Licence at `http://www.coastalmonitoring.org`.

than a surface-following sensor to severe weather impacts or the influence of marine traffic (although bottom-trawling by fishing vessels can present problems). Since it can also be used to measure currents, such an instrument is particularly beneficial for studies of wave-current interaction. Some researchers have assessed the accuracy of wave measurements by ADCPs compared with wave buoys. Bouferrouk et al. [5] compared the wave data collected by a 5-beam ADCP and 4 wave buoys at the WaveHub (UK) - a site that is dedicated to the testing of wave energy devices. Their results show, in general, good agreement between ADCP and wave buoys. However, unlike wave buoys, the 5-beam ADCP could also detect long period swell waves (0.07-0.08 Hz), for small wave heights.

Remote Sensing

Remote sensing generally refers to observations made at some distance from the medium that is being observed. This can involve the use of satellite sensors, instruments carried by aircraft ('airborne remote sensing'), or installed on land- or sea-based platforms (e.g. X-band and HF radar).

Remote sensing can be categorised as either *passive* or *active*. Passive sensors gather radiation that has been emitted or reflected by the sea surface, for example reflected sunlight. In contrast, active sensors emit energy, then detect the radiation that is reflected or backscattered from the target. An example of an active sensor is radar: we shall discuss two types of wave measuring radar technology.

Marine X-band radar is a well-established technology for navigation and collision avoidance, and can be found on most large research vessels, and on many offshore installations. X-band is a segment of the microwave radio region of the electromagnetic spectrum, with a frequency range $8 - 12$ GHz and a wavelength of around 3cm. The images produced by marine radars detect not only hard targets such as ships and coastlines, but also reflections from the sea surface, known as 'sea clutter' [3] caused by small, wind-induced ripples. The backscatter from this rough surface reveals the underlying shape of the waves. With the correct software, it is possible to analyse this signal to gain information on the wave and current regime.

X-band radar systems can scan the ocean surface at a range of a few kilometres, with sufficiently high temporal and spatial resolution to resolve individual waves, and can relay the signals in real time. An area of sea surface of several square kilometres can therefore be continuously monitored. X-band radar systems can be installed on moving vessels or on fixed platforms offshore or at coastal sites (although the requirement for proximity to the area of interest can present practical challenges).

The radar system outputs a two-dimensional image (such as that shown in Figure 11.19), providing information about spatial variability and directionality of waves and currents (including full directional spectra) which is not available from a point sensor such as a buoy or an AWAC. Wave length and wave period are straightforward to measure, and the wave dispersion relation can then

be used to deduce information about surface currents and bathymetry [18]. However, since the radar image is a two-dimensional projection of the three-dimensional sea surface, direct waveheight information is trickier to obtain, and an additional sensor such as a buoy is often required for waveheight calibration. Figure 11.19 shows an area of sea being monitored by an X-band radar situated in a lighthouse at the Butt of Lewis, Scotland, with a buoy located nearby for calibration.

Analysis of the radar signal for a robust surface elevation estimate is currently an active research area, due to the potential for X-band monitoring to offer insights into wave-tide interactions and wave transformations in complex bathymetries. An in-situ radar system providing real-time data also has the potential to be used for short-term wave prediction, useful for control and maintenance of devices.

Another remote sensing technology is High Frequency (HF) radar, which derives information from the Doppler shift of transmitted and reflected signals, and can calculate full directional spectra. Operating at much lower frequencies ($3 - 30$ MHz) than X-band allows the range for sampling to reach 100km [31] although the longer wavelength leads to coarser resolution, typically between 1km and 5km. Surface currents can also be estimated, and the system can also be used to measure the vertical distribution of winds *via* a radar wind profiler. In contrast to X-band, HF radar systems require considerable and costly infrastructure installation with two transmitter/receiver stations to receive signals at right angles. NOAA has set up a network of HF radar systems around the US coast (`ioos.noaa.gov/project/hf-radar/`) for real time monitoring of coastal currents.

11.4.2 Modelling the Wave Resource

Hindcast wave resource models are used for:

- Site selection for devices (with the scope and detail depending on the stage of the project);
- Predicting long term energy yield for devices (robust, standardised procedures will support the investment case for deployment);
- Device design and optimisation;
- Estimating extreme conditions for survivability;
- Determining the impacts of the proposed device on the physical environment.

The models will elucidate the spatial distribution and temporal variation of wave energy, including seasonal and annual averages, with simulations usually run for a ten year period and validated with in-situ measurements for sample locations and durations. Wave resource assessments can be classed into three levels of fidelity: reconnaissance, feasibility and design. Accuracy and resolution

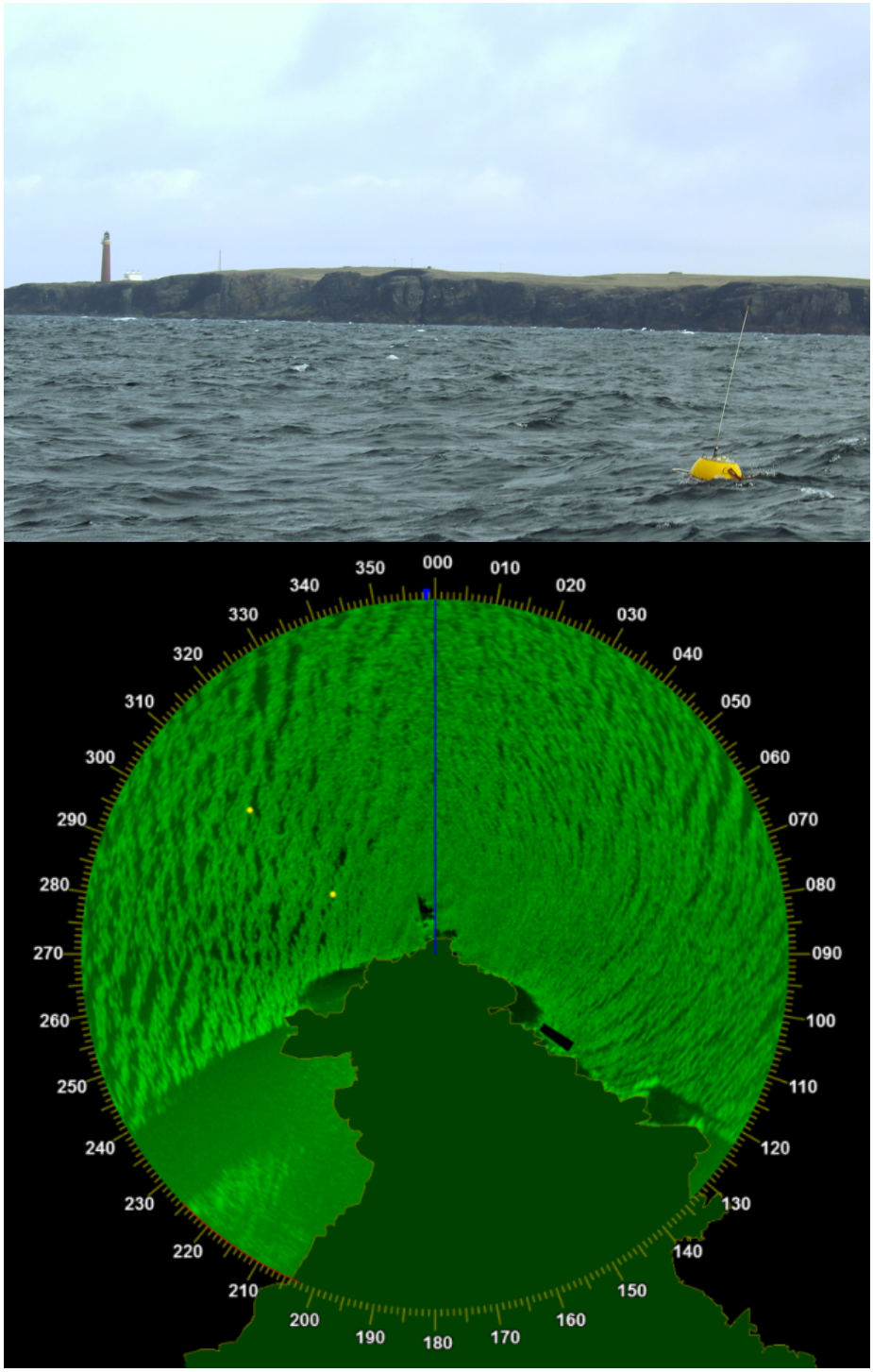

Figure 11.19: An area of sea around the Butt of Lewis Lighthouse in the Isle of Lewis, Scotland being monitored with X-band radar. The X-band system is housed in the lighthouse (top image), with a Datawell Waverider MkIII in situ for calibration of waveheight. The resulting radar backscatter measurements (bottom image) allow waves to be resolved over a 3km radius. Photographs courtesy of Arne Vögler.

Class	1	2	3
Name	Reconnaissance	Feasibility	Design
Purpose	Areas of interest	Resource description	WEC locations
Longshore Extent	>300km	20km-500km	<25km
Resolution	5km, 3hrs	500m, 3hrs	50m, 1hr
Uncertainty in H_{m0}, J and T_e	20%	10%	7%
Uncertainty in θ_{Jmax}	-	15°	7°
Uncertainty in ε_0 and d	-	25%	15%

Table 11.4: Dependence of typical domain size, recommended spatial and temporal resolution and maximum uncertainty of model outputs on the level of resource assessment [20]. The main output parameters H_{m0}, J and T_e are significant waveheight, omnidirectional power and energy period respectively. Feasibility and design level models also require direction of maxiumum directionally resolved wave power θ_{Jmax}, spectral width ε_0 and directionality coefficient d. The model extent also depends on the availability and location of boundary data.

of input data and simulation are progressively increased at each stage, as shown in Table 11.4.

Wave models can be classed as deterministic (phase resolving) or spectral (phase averaged). Phase resolving models are similar in spirit to computational fluid dynamics, with rigorous implementation of the field equations yielding the evolution of the sea surface in the time domain. The input is usually the surface elevation time histories at the boundary location, or a full spatial description of the initial elevation and velocity. These models can be useful for very localised simulation (for example around structures), and can be helpful for developers of shoreline wave energy converters. However, since the surface elevation can vary rapidly in space and time, such models would be too computationally intensive for larger domains or longer time periods, even if suitable boundary information were available at such scales.

Instead, the vast majority of numerical wave software for resource assessment consists of phase averaged spectral wave simulations. Such models track the evolution of the directional wave spectrum at each node across the domain. Quantities derived from this spectrum offer a statistical description of the wave conditions in time and space. Since wave spectra vary much more gradually than time domain quantities, simulation codes can cope with much larger spatial and temporal extents than phase-resolving models, and do not need such precise boundary conditions. This makes them ideal for resource modelling. Parameters calculated from the output spectra, such as significant waveheight

and energy period, give a universally understood method of characterising the wave climate, and their joint probability statistics in a given location can be used in conjunction with a device's power matrix to predict yield.

A spectral resolution of at least 25 frequencies (between 0.033Hz and 0.5Hz) by 24 directions is recommended by the IEC [20] for wave resource modelling, though a finer directional resolution may sometimes be required, with resolutions of $2^\circ - 5^\circ$ recommended to correctly model coastal swell waves in SWAN [2]. As described in 11.2.1, simulations can be conducted across either structured grids (which will then involve nesting if higher resolutions are required in a particular location) or unstructured (in which case the mesh resolution can be adjusted to concentrate on areas of interest, and also to maintain accuracy and stability in areas of rapidly changing bathymetry or around obstacles such as islands). Spectral wave models track the evolution of wave spectra using the Wave Action Conservation Equation [21]:

$$\sigma \left\{ \frac{\partial}{\partial t} \left(N(\mathbf{x}, \sigma, \theta, t) \right) + \nabla . \left[\mathbf{v} N(\mathbf{x}, \sigma, \theta, t) \right] \right\} = \begin{array}{cc} S_{\text{wind}} & \text{Wind Forcing} \\ +S_{\text{wcap}} & \text{Whitecapping} \\ +S_{\text{bot}} & \text{Bottom Friction} \\ +S_{\text{surf}} & \text{Wavebreaking} \\ +S_{\text{nl}} & \text{Nonlinear Interactions} \end{array} \tag{11.28}$$

The action density $N(\mathbf{x}, \sigma, \theta, t)) = \frac{E(\mathbf{x}, \sigma, \theta, t))}{\sigma}$, where $E(\mathbf{x}, \sigma, \theta, t)$ is the depth-integrated energy density, σ is frequency, θ is direction, and $\mathbf{x}$ is position. The propagation velocity $\mathbf{v}$ and differential operator ∇ act in four-dimensional phase space, consisting of two spatial dimensions (such as latitude and longitude) and two spectral dimensions (such as frequency and direction). The $\nabla.(\mathbf{v}N)$ term includes shoaling, depth- and current-induced refraction, and can be modified to incorporate diffraction.

Relevant physical phenomena which generate, dissipate or redistribute energy appear as source terms on the right hand side of (11.28): energy input through wind forcing, dissipation by whitecapping, bottom friction, depth-induced wavebreaking, and nonlinear quadruplet and triad interactions. These mechanisms will be considered in turn later in this section. Their relative importance in different types of ocean model is shown in Table 11.5.

The numerical solution of (11.28), without any prior assumption about the spectral shape, is known as a *third generation* wave model [14], is implemented in software such as SWAN [4], WAM [14], and WAVEWATCH III [40], and is the recommended model for all levels of wave energy resource assessment [20].

The remainder of the section will discuss the implementation of these models in more detail. We will move progressively shorewards from the deepwater extremities of the model. After considering the appropriate boundary conditions, we will turn to the energy exchange mechanisms that are the most significant in deep water, namely wind input and whitecapping dissipation. Following a discussion of nonlinear interactions, we will then consider how to ensure interactions with the bottom are correctly included by discussing bathymetry data, bottom friction and depth-induced wavebreaking.

	Deep Oceans	Shelf Seas	Shoaling Zone	Harbours
Diffraction	1	1	2	4
Refraction/Shoaling	1	3	4	3
Current Refraction	1	2	3	1
Quad Interactions	4	4	2	1
Triad Interactions	1	2	3	2
Atmospheric Input	4	4	2	1
Whitecapping	4	4	2	1
Depth Induced Breaking	1	2	4	1
Bottom Friction	1	4	2	1

Key:

1: negligible
2: minor importance
3: significant
4: dominant

Table 11.5: Relative importance of physical processes in ocean wave models [42]

Boundary Conditions

Unless a whole ocean or sea is to be simulated, the wave conditions at the boundary must be prescribed. Although parametric boundary data can be used for a reconnaissance model, feasibility and design models require timeseries of two-dimensional frequency-directional spectra. These should cover the whole time period under investigation, with a temporal resolution to match that of the model itself. It is desirable (particularly from a practical standpoint) to place offshore boundaries in regions where the wave conditions are fairly homogeneous, e.g. away from islands or sudden changes in bathymetry.

In theory, one can use physically recorded boundary data. However, this would require ten years worth of data (and in the form of directional spectra, which cannot be calculated from buoys and AWACs without additional assumptions) with a recommended return rate of 70% [20]. Furthermore, data from a single point sensor may not be suitable for a large offshore boundary with spatial variability. Therefore, most models use the outputs from larger "parent" models as boundary conditions. These can be taken from earlier levels of (validated) resource assessment, nested models, or external global modelled datasets such as ECMWF ERA-5 [17]. If there is spatial variation in the boundary conditions, this should be included in the model. This is easily done in successive nested models in codes such as SWAN, or else boundaries can be divided into smaller segments to be treated separately if required.

When generating boundary conditions, it may be helpful to run a short duration model with an output location situated close to the driving boundary, to verify that the boundary condition is being correctly implemented.

Closed boundaries, such as land, absorb incoming waves and produce no

outgoing waves. Closed boundaries may also be used at the lateral edges of coastal models, where only the offshore boundary is prescribed. In this case, it is advisable to ensure the boundary is sufficiently far from the area of interest by moving its position and verifying that the change does not affect the output. Some codes such as DHI Mike21 SW [12] have an additional option for lateral boundaries (particularly if they are relatively straight and perpendicular to depth contours), where a one-dimensional form of the basic transport equations is solved to create intermediate wave spectra along the edge of the model area from the offshore boundary to land.

Wind and Whitecapping

The source terms in (11.28) reflect a balance between energy loss due to physical processes such as whitecapping, and energy input through wind. The importance of the wind will depend on the size of the model. Large scale models (such as the whole Atlantic) may be driven entirely from wind data [26]. However, even in smaller models, the spectra will decay across the domain without the inclusion of wind.

The wind input across the frequency spectrum is modelled using a linear growth term proportional to the wind speed, and an exponential contribution which also depends on surface roughness and hence seastate. Wind should be specified as U_{10}, the wind velocity 10m above sea level. Suggested resolutions for wind input are shown in 11.6. It has been estimated that a 10% error in wind can lead to a 20% error in waveheight, depending on the size of the model [12].

	Reconnaissance	Feasibility	Design
Temporal	3h	3h	1h
Spatial	100km	25km	5km

Table 11.6: Recommended resolutions for wind data

Energy dissipation by *whitecapping* can also have a significant influence, particularly in large regions of shelf sea and open ocean. The source term most commonly used in spectral wave models is [21]

$$S_{\mathrm{wcap}}(\sigma,\theta) = -C_{\mathrm{ds}}\frac{\hat{\alpha}}{\hat{\alpha}_{PM}}^{4}\left\{(1-\delta)\frac{k}{\bar{k}}+\delta\left(\frac{k}{\bar{k}}\right)^{2}\right\}\bar{\sigma}E(\sigma,\theta) \tag{11.29}$$

where the wave steepness $\hat{\alpha} = \bar{k}\sqrt{E_{\mathrm{tot}}}$, k is the wave number, σ the relative frequency and $\hat{\alpha}_{PM}$ is a reference value for the Pierson-Moskowitz spectrum. The constant C_{ds} fixes overall amount of dissipation while δ determines the part of the spectrum most affected. These constants may be tuned in a calibration process to improve model performance: C_{dis} will have a greater influence on significant waveheight while δ will affect mean wave period and energy period.

Nonlinear Interactions

Nonlinear wave-wave interactions redistribute wave energy over the spectrum, due to an exchange of energy resulting from resonant sets of wave components. In wave models, two such processes are particularly important: four-wave interactions in deep and intermediate waters (known as *quadruplets*), and three-wave interactions in shallow water (*triads*). A good explanation of the principle of non-linear wave-wave interactions is provided by Holthuijsen [19]. To visualise the triad interaction, consider two wave paddles, generating waves of different frequencies and directions, placed in two corners along one side of a tank of constant water depth. The resulting waves create a diamond pattern of crests and troughs, which has its own wave length, speed and direction. This diamond pattern would interact with a third wave component which had the same wave length, speed and direction, redistributing wave energy within the spectrum due to resonance. Although each of the individual wave components can gain or lose energy, the sum of the energy at each point in the tank would remain constant.

These triad interactions do not occur in deep water, since the resonant conditions (i.e. matching of wave speed, length and direction) cannot be met. However, two pairs of wave components in deep water can interact with each other in a quadruplet wave-wave interaction.

Quadruplets transfer wave energy in deep water from the peak frequency outwards to lower frequencies (shifting the peak downwards) as well as higher frequencies (leading to dissipation by whitecapping), whereas triads transfer energy from lower to higher frequencies, and transform single peaked spectra into multiple peaked spectra as they approach the shore. Both are included as source terms in third generation wave models, and it is noted that both are computationally expensive. It is common practice (and the default configuration in SWAN) to omit triads but include quadruplet interactions.

The Seabed

As waves move from deep to shallower waters, the morphology and composition of the seabed becomes increasingly important in determining the spatial dependence of the wave climate. Bathymetry datasets of appropriate resolution are required to adequately capture wave shoaling and refraction. The recommended maximum horizontal spacing of bathemetric data for different stages of resource assessment are given in Table 11.7. In addition, the depth level should not change too abruptly between adjacent points. The maximum difference in water depth between data points is 10% for reconnaissance models, 5% for feasibility models and 2% for design models. Existing datasets such as GEBCO (`www.gebco.net`) can be used for a reconnaissance model, but new surveys may have to be commissioned for later stages.

Bathymetry is not the only factor determining water depth: depending on the location, the tidal range can cause variations in depth of up to 16m, modulating the wave behaviour. If a model sensitivity analysis indicates that it is required, the water level should be prescribed for each timestep. For most appli-

Depth	Reconnaissance	Feasibility	Design
>200m	5km	2km	1km
20m - 200m	500m	100m	25m
<20m	100m	50m	10m

Table 11.7: Recommended maximum horizontal spacing of bathymetric data from [20]

cations, a single water level timeseries applied across the whole spatial domain will suffice. In areas where tidal currents may also have a significant effect on wave propagation, it would be advisable to run a further sensitivity analysis to determine whether these should be included in the model, by including external current data or coupling to a hydrodynamic model.

As waves reach shallower water, the orbital velocities penetrate the water depth and the dissipation term in (11.28) due to frictional wave-bottom interaction comes into play. The dissipation rate may be expressed as [38]

$$S_{bot}(\sigma,\theta) = -C_b \frac{\sigma^2}{g^2 \sinh^2 kd} E(\sigma,\theta) \tag{11.30}$$

where C_b is a bottom friction coefficient, can be determined according to either an empirical model [16], a drag law model [11] or an eddy-viscosity formulation [23]. Simulation codes such as SWAN and Mike21 allow the user to select one of these bottom friction models, each of which incorporates a scaling coefficient which can be chosen by the user. This can be chosen by attempting to parametrise the roughness of the seabed at the location in question, but is more usually obtained by a calibration process.

As waves propagate further into shallow water, wave shoaling leads to an increase in wave height. Waves tend to steepen at the front and to become more gently sloping at the back. When the waves reach water which is so shallow that the wave height can no longer be supported by the water depth, they will break. This occurs when the particle velocities at the crest exceed the phase speed, or when the free-surface becomes vertical. Depth-induced wave breaking is included as a source term in third generation wave models:

$$S_{\text{surf}}(\sigma,\theta) = -\frac{\alpha Q_b \bar{\sigma} H_{max}^2}{8\pi} \frac{E(\sigma,\theta)}{E_{\text{tot}}} \tag{11.31}$$

where $\alpha_0 \simeq 1$ is the rate of dissipation, Q_b is the fraction of breaking waves, $\bar{\sigma}$ is the mean relative frequency, and E_{tot} is the total energy. The maximum wave height $H_{max} = \gamma h$ where h is the depth and the parameter γ may be chosen by calibration if the area of interest is shallow enough to require detailed consideration of depth-induced wavebreaking effects.

Acknowledgements

David Christie and Simon Neill acknowledge the support of SEEC (Smart Efficient Energy Centre) at Bangor University, part-funded by the European Regional Development Fund (ERDF), administered by the Welsh Government.

Bibliography

[1] ABPmer. Atlas of UK marine renewable energy resources: Atlas pages. *A strategic environmental assessment report, Department for Business Entreprise & Regulatory Reform*, 2008.

[2] Richard Allard, Erick Rogers, and Suzanne Carroll. *User's Manual for the Simulating Waves Nearshore Model (SWAN)*. Delft University of Technology, 2002.

[3] Paul S Bell, John Lawrence, and Jennifer V Norris. Determining currents from marine radar data in an extreme current environment at a tidal energy test site. In *2012 IEEE International Geoscience and Remote Sensing Symposium*, pages 7647–7650. IEEE, 2012.

[4] N Booij, RC Ris, and Leo H Holthuijsen. A third-generation wave model for coastal regions: 1. Model description and validation. *Journal of Geophysical Research: Oceans*, 104(C4):7649–7666, 1999.

[5] Abdessalem Bouferrouk, Jean-Baptiste Saulnier, George H Smith, and Lars Johanning. Field measurements of surface waves using a 5-beam ADCP. *Ocean Engineering*, 112, 2016.

[6] P.A. Brodtkorb, P. Johannesson, G. Lindgren, I. Rychlik, J. Rydén, and E. Sjö. WAFO - a Matlab toolbox for the analysis of random waves and loads. In *Proc. 10'th Int. Offshore and Polar Eng. Conf., ISOPE, Seattle, USA*, volume 3, pages 343–350, 2000.

[7] Loren Carrère, Florent Lyard, M Cancet, A Guillot, and Laurent Roblou. FES2012: A new global tidal model taking advantage of nearly 20 years of altimetry. In *Proceedings of meeting*, volume 20, 2012.

[8] Changsheng Chen, Hedong Liu, and Robert C Beardsley. An unstructured grid, finite-volume, three-dimensional, primitive equations ocean model: application to coastal ocean and estuaries. *Journal of Atmospheric and Oceanic Technology*, 20(1):159–186, 2003.

[9] David Christie. Maxentropyspt github package. `https://github.com/davidcchristie/MaxEntropySPT`, 2020.

[10] Mary A Cialone, T Chris Massey, Mary E Anderson, Alison S Grzegorzewski, Robert E Jensen, Alan Cialone, David J Mark, Kimberly C Pevey, Brittany L Gunkel, and Tate O McAlpin. North atlantic coast comprehensive study (naccs) coastal storm model simulations: Waves and water levels. Technical report, ENGINEER RESEARCH AND DEVELOPMENT CENTER VICKSBURG MS COASTAL AND HYDRAULICS LAB, 2015.

[11] J Ian Collins. Prediction of shallow-water spectra. *Journal of Geophysical Research*, 77(15):2693–2707, 1972.

[12] DHI. *Mike21 Spectral Wave User Manual*. `https://www.mikepoweredbydhi.com/`.

[13] Gary D Egbert and Svetlana Y Erofeeva. Efficient inverse modeling of barotropic ocean tides. *Journal of Atmospheric and Oceanic technology*, 19(2):183–204, 2002.

[14] The Wamdi Group. The WAM model - a third generation ocean wave prediction model. *Journal of Physical Oceanography*, 18(12):1775–1810, 1988.

[15] Hashimoto and Kobune. Estimation of directional spectra from the maximum entropy principle. In *Proceedings of the 5th International Offshore Mechanics and Arctic Engineering Symposium, Tokyo*, pages 80–85, 1986.

[16] Klaus Hasselmann, Tim P Barnett, E Bouws, H Carlson, David E Cartwright, K Enke, JA Ewing, H Gienapp, DE Hasselmann, P Kruseman, et al. Measurements of wind-wave growth and swell decay during the joint north sea wave project (jonswap). *Ergänzungsheft 8-12*, 1973.

[17] Hans Hersbach, Bill Bell, Paul Berrisford, Shoji Hirahara, András Horányi, Joaquín Muñoz-Sabater, Julien Nicolas, Carole Peubey, Raluca Radu, Dinand Schepers, Adrian Simmons, Cornel Soci, Saleh Abdalla, Xavier Abellan, Gianpaolo Balsamo, Peter Bechtold, Gionata Biavati, Jean Bidlot, Massimo Bonavita, Giovanna De Chiara, Per Dahlgren, Dick Dee, Michail Diamantakis, Rossana Dragani, Johannes Flemming, Richard Forbes, Manuel Fuentes, Alan Geer, Leo Haimberger, Sean Healy, Robin J. Hogan, Elías Hólm, Marta Janisková, Sarah Keeley, Patrick Laloyaux, Philippe Lopez, Cristina Lupu, Gabor Radnoti, Patricia de Rosnay, Iryna Rozum, Freja Vamborg, Sebastien Villaume, and Jean-Noël Thépaut. The era5 global reanalysis. *Quarterly Journal of the Royal Meteorological Society*, 146(730):1999–2049, 2020.

[18] Katrin Hessner, Konstanze Reichert, Jose Carlos Nieto Borge, Craig L Stevens, and Murray J Smith. High-resolution x-band radar measurements of currents, bathymetry and sea state in highly inhomogeneous coastal areas. *Ocean Dynamics*, 64(7):989–998, 2014.

[19] Leo H Holthuijsen. *Waves in oceanic and coastal waters*. Cambridge University Press, 2010.

[20] International Electrotechnical Commission. *Marine energy - Wave, tidal and other water current converters - Part 101: Wave energy resource assessment and characterization*, iec 62600-101 ts edition.

[21] G. J. Komen, L. Cavaleri, M. Donelan, K. Hasselmann, S. Hasselmann, and P. A. E. M. Janssen. *Dynamics and Modelling of Ocean Waves*. Cambridge University Press, 1994.

[22] Michael S. Longuet-Higgins, D. E. Cartwright, and N. D. Smith. Observations of the directional spectrum of sea waves using the motions of a floating buoy. In *Ocean Wave Spectra, proceedings of a conference, Easton, Maryland*, pages 111–136. National Academy of Sciences, Prentice-Hall, 1963.

[23] OS MADSEN. Spectral wave attenuation by bottom friction: Theory. In *Proc. 21st Int. Conf. Coastal Eng.*, pages 492–504, 1988.

[24] George L Mellor, Tal Ezer, and Lie-Yauw Oey. The pressure gradient conundrum of sigma coordinate ocean models. *Journal of atmospheric and oceanic technology*, 11(4):1126–1134, 1994.

[25] L Mentaschi, G Besio, F Cassola, and A Mazzino. Problems in RMSE-based wave model validations. *Ocean Modelling*, 72:53–58, 2013.

[26] Simon P Neill and M Reza Hashemi. Wave power variability over the northwest European shelf seas. *Applied energy*, 106:31–46, 2013.

[27] Simon P Neill, M Reza Hashemi, and Matt J Lewis. The role of tidal asymmetry in characterizing the tidal energy resource of Orkney. *Renewable Energy*, 68:337–350, 2014.

[28] Simon P Neill, Emmer J Litt, Scott J Couch, and Alan G Davies. The impact of tidal stream turbines on large-scale sediment dynamics. *Renewable Energy*, 34(12):2803–2812, 2009.

[29] SP Neill and AJ Elliott. In situ measurements of spring–neap variations to unsteady island wake development in the Firth of Forth, Scotland. *Estuarine, Coastal and Shelf Science*, 60(2):229–239, 2004.

[30] NOAA. WAVEWATCH III - National Weather Center. `http://polar.ncep.noaa.gov/waves/index2.shtml`, 2016. Accessed: 04-01-2017.

[31] E Pitt. Assessment of Wave Energy Resource. *EMEC British Standards Institution*, 2009.

[32] Victor Ramos and John V Ringwood. Implementation and evaluation of the International Electrotechnical Commission specification for tidal stream energy resource assessment: A case study. *Energy Conversion and Management*, 127:66–79, 2016.

[33] RD Instruments. Principles of operation a practical primer. *Available from RDInstruments.com*, 1996.

[34] Peter E Robins, Simon P Neill, Luis Giménez, Stuart R Jenkins, and Shelagh K Malham. Physical and biological controls on larval dispersal and connectivity in a highly energetic shelf sea. *Limnology and Oceanography*, 58(2):505–524, 2013.

[35] Peter E Robins, Simon P Neill, and Matt J Lewis. Impact of tidal-stream arrays in relation to the natural variability of sedimentary processes. *Renewable Energy*, 72:311–321, 2014.

[36] Alexander F Shchepetkin and James C McWilliams. The regional oceanic modeling system (ROMS): a split-explicit, free-surface, topography-following-coordinate oceanic model. *Ocean Modelling*, 9(4):347–404, 2005.

[37] David A Sutherland, Parker MacCready, Neil S Banas, and Lucy F Smedstad. A model study of the Salish Sea estuarine circulation. *Journal of Physical Oceanography*, 41(6):1125–1143, 2011.

[38] SWAN Team and others. SWAN Scientific and Technical Documentation, SWAN Cycle III version 40.81. *Delft University of Technology*, 2010.

[39] Kristen M Thyng, James J Riley, and Jim Thomson. Inference of turbulence parameters from a ROMS simulation using the k-ε closure scheme. *Ocean Modelling*, 72:104–118, 2013.

[40] Hendrik L Tolman, Bhavani Balasubramaniyan, Lawrence D Burroughs, Dmitry V Chalikov, Yung Y Chao, Hsuan S Chen, and Vera M Gerald. Development and implementation of wind-generated ocean surface wave modelsat NCEP. *Weather and forecasting*, 17(2):311–333, 2002.

[41] Roxana C Wajsowicz. A consistent formulation of the anisotropic stress tensor for use in models of the large-scale ocean circulation. *Journal of Computational Physics*, 105(2):333–338, 1993.

[42] I.R. Young. *Wind Generated Ocean Waves*. ISSN. Elsevier Science, 1999.